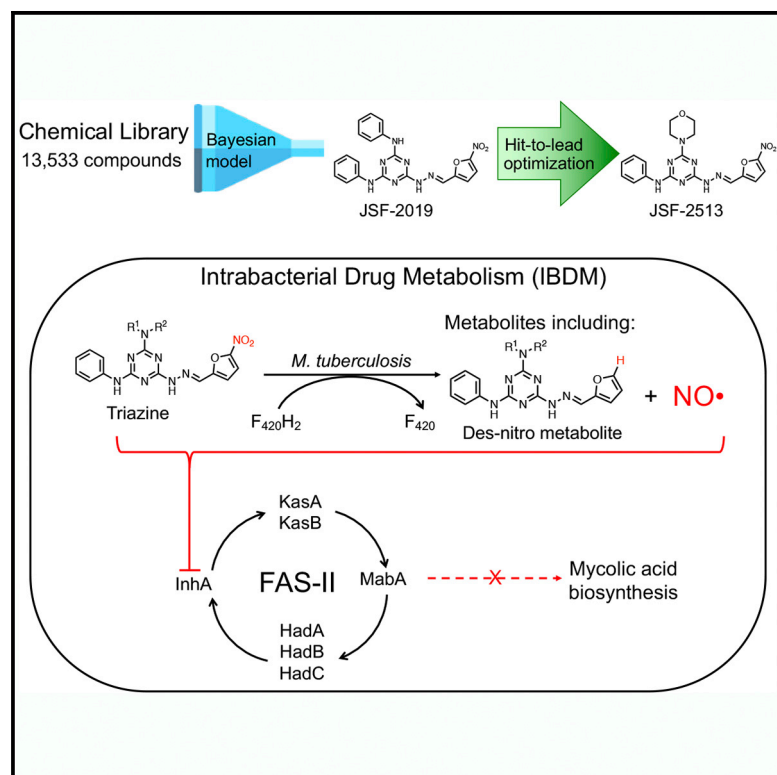


Cell Chemical Biology

Antitubercular Triazines: Optimization and Intrabacterial Metabolism

Graphical Abstract



Authors

Xin Wang, Daigo Inoyama,
Riccardo Russo, ..., Nancy Connell,
Pradeep Kumar, Joel S. Freundlich

Correspondence

freundjs@rutgers.edu

In Brief

Wang et al. disclose the optimization of a triazine antitubercular agent and probe its mechanism of action. They demonstrate the significance of studying intrabacterial drug metabolism. Through this approach and other methods, they evidence a novel mechanism involving $NO^•$ release and inhibition of the cell wall biosynthesis enzyme *InhA*.

Highlights

- Optimization of an antitubercular agent afforded gains in solubility and plasma PK
- The triazines release intrabacterial $NO^•$ as the predominant mechanism of action
- The triazines/their intrabacterial metabolites also inhibit *InhA* and FAS-II pathway



Antitubercular Triazines: Optimization and Intrabacterial Metabolism

Xin Wang,^{1,7} Daigo Inoyama,^{1,7} Riccardo Russo,² Shao-Gang Li,¹ Ravindra Jadhav,¹ Thomas P. Stratton,¹ Nisha Mittal,¹ Joseph A. Bilotta,¹ Eric Singleton,² Thomas Kim,² Steve D. Paget,¹ Richard S. Pottorf,¹ Yong-Mo Ahn,¹ Alejandro Davila-Pagan,¹ Srinivasan Kandasamy,¹ Courtney Grady,² Seema Hussain,^{3,4} Patricia Soteropoulos,^{3,4} Matthew D. Zimmerman,⁵ Hsin Pin Ho,⁵ Steven Park,⁵ Véronique Dartois,⁵ Sean Ekins,⁶ Nancy Connell,² Pradeep Kumar,² and Joel S. Freundlich^{1,2,8,*}

¹Department of Pharmacology, Physiology and Neuroscience, Rutgers University – New Jersey Medical School, Newark, NJ 07103, USA

²Division of Infectious Disease, Department of Medicine and the Ruy V. Lourenço Center for the Study of Emerging and Re-emerging Pathogens, Rutgers University – New Jersey Medical School, Newark, NJ 07103, USA

³Genomics Center, Rutgers University – New Jersey Medical School, Newark, NJ 07103, USA

⁴Department of Microbiology, Biochemistry and Molecular Genetics, Rutgers University – New Jersey Medical School, Newark, NJ 07103, USA

⁵Public Health Research Institute, Rutgers University – New Jersey Medical School, Newark, NJ, USA

⁶Collaborations in Chemistry Inc., Raleigh, NC 27606, USA

⁷These authors contributed equally

⁸Lead Contact

*Correspondence: freundjs@rutgers.edu

<https://doi.org/10.1016/j.chembiol.2019.10.010>

SUMMARY

The triazine antitubercular JSF-2019 was of interest due to its *in vitro* efficacy and the nitro group shared with the clinically relevant delamanid and pretomanid. JSF-2019 undergoes activation requiring $F_{420}H_2$ and one or more nitroreductases in addition to Ddn. An intrabacterial drug metabolism (IBDM) platform was leveraged to demonstrate the system kinetics, evidencing formation of NO^{\cdot} and a des-nitro metabolite. Structure-activity relationship studies focused on improving the solubility and mouse pharmacokinetic profile of JSF-2019 and culminated in JSF-2513, relying on the key introduction of a morpholine. Mechanistic studies with JSF-2019, JSF-2513, and other triazines stressed the significance of achieving potent *in vitro* efficacy via release of intrabacterial NO^{\cdot} along with inhibition of *InhA* and, more generally, the FAS-II pathway. This study highlights the importance of probing IBDM and its potential to clarify mechanism of action, which in this case is a combination of NO^{\cdot} release and *InhA* inhibition.

INTRODUCTION

Mycobacterium tuberculosis is the causative agent of tuberculosis, the world's deadliest infectious disease. The World Health Organization's most recent report revealed 10 million cases and 1.6 million mortalities for 2017 (WHO, 2018). The need for new drugs is underscored by criteria such as (1) lack of cross-resistance with existing therapies and (2) potential for shortening therapy from ca. 6 months and 2 years for drug-sensitive and

drug-resistant infections, respectively. The newest additions to the tuberculosis drug armamentarium consist of bedaquiline (approved by the Food and Drug Administration [FDA] in 2012), pretomanid (approved by the FDA in 2019; Figure 1A), and delamanid (approved by the European Medicines Agency in 2014; Figure 1B). While bedaquiline inhibits ATP biosynthesis (Andries et al., 2005), delamanid, or OPC-67683, appears to target *M. tuberculosis* through the release of nitric oxide (NO^{\cdot}) as well as inhibition of cell wall biosynthesis, more specifically through modulating mycolic acid biosynthesis through an apparent reduction in ketomycolates (Matsumoto et al., 2006). However, concerns with delamanid have been raised over poor bioavailability, additive QTc prolongation, and marginally shortened duration for culture conversion when co-administered with an optimized background regimen in a pivotal phase 3 trial (Geiter, 2017). Pretomanid, the most recently approved drug, seems to function through a mechanism of action similar to that of delamanid (Manjunatha et al., 2006, 2009; Singh et al., 2008; Stover et al., 2000), with superior bactericidal activity. Pretomanid offers promise as a highly effective oral, short-course regimen for multidrug and extensively drug-resistant infections when co-administered with bedaquiline and linezolid (Conradie et al., 2017; Murray, 2016). Both delamanid and pretomanid are nitro-containing heterocycles, which do not cause genotoxicity. In fact, the Ames mutagenicity of the parent of pretomanid (CGI-17341) (Ashtekar et al., 1993) and early analogs were attributed to metabolic oxidation of the benzyl methylene group (Thompson et al., 2011). Both pretomanid and delamanid suffer from significant liabilities due to a relatively high frequency of resistance (FOR) ($\sim 10^{-5}$ – 10^{-6}) and any one of these mutations leads to a dramatic loss of potency (≥ 500 -fold). In clinical studies where pretomanid is combined with other antituberculars, pretomanid resistance remains a significant issue (Harper et al., 2012; Li et al., 2017). It is clear that pretomanid and delamanid are not ideal additions to the tuberculosis drug



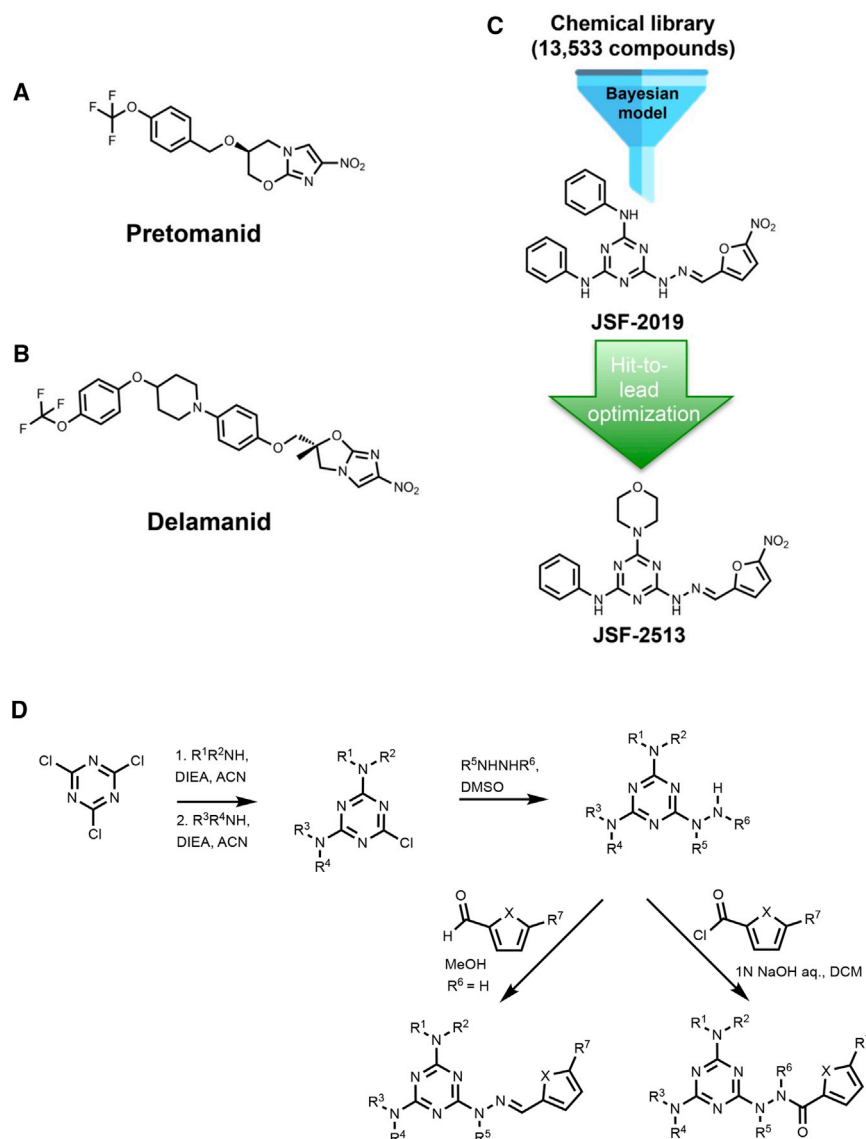


Figure 1. Highlighted Chemical Structures and Reaction Chemistry

Chemical structures of (A) pretomanid and (B) delamanid, and (C) the evolution from JSF-2019 to JSF-2513 enabled by (D) a facile synthetic route. Chemical structures of pretomanid and delamanid are depicted in (A) and (B), respectively. (C) The evolution of the triazine series from the initial Bayesian model hit JSF-2019 to JSF-2513. (D) The general route involved sequential amine additions to cyanuric chloride. The hydrazine was then added and capped with either an aldehyde to afford the hydrazones or an acid chloride to prepare the acyl hydrazides.

exhibiting a minimum bactericidal concentration (MBC; lowest concentration to reduce the bacterial population by 2 log₁₀) of 600–1,200 nM. Profiling of JSF-2019 demonstrated a lack of cross-resistance with front-line drugs and a smaller loss of whole-cell efficacy versus pretomanid-resistant mutants (Ekens et al., 2013; Inoyama et al., 2018). However, JSF-2019 lacked *in vivo* efficacy in models of acute *M. tuberculosis* infection model (Bruhin et al., 1969; Ekins et al., 2013), which has been attributed to a sub-optimal mouse PK profile (area under the curve [AUC_{0–5h}] = 1,148 h*ng/mL based on a single 25-mg/kg oral dose as measured in the plasma) (Inoyama et al., 2018). The PK profile may be driven by poor aqueous solubility ($S < 0.060 \mu\text{M}$ < goal of at least 1 μM) (Inoyama et al., 2018).

Here, we disclose the optimization of JSF-2019 to enhance triazine solubility and mouse PK profile to arrive at JSF-2513, which features a critical morpholine moiety. We also explored the mechanism

of action of these triazines, focusing primarily on JSF-2019 and the optimized analog JSF-2513 (Figure 1C), and demonstrated the significance of the intrabacterial F₄₂₀H₂-dependent release of nitric oxide (NO[•]) and the inhibition of the essential enoyl-acyl carrier protein reductase InhA. These results offer insights of value to the pursuit of next-generation nitro-containing antituberculars to supplant pretomanid and/or delamanid.

regimen and, therefore, efforts are ongoing to arrive at a replacement by addressing issues with *in vitro* and *in vivo* efficacy and pharmacokinetic (PK) profile (Blaser et al., 2012; Palmer et al., 2015; Thompson et al., 2017). Our laboratory serendipitously entered the realm of nitro-substituted heterocyclic antituberculars with the rediscovery of the whole-cell growth-inhibitory efficacy of (*E*)-6-(2-((5-nitro-furan-2-yl)methylene)hydrazinyl)-N2,N4-diphenyl-1,3,5-triazine-2,4-diamine (JSF-2019; Figure 1C) (Ekens et al., 2013). Predicted by our naive Bayesian dual-event model, it was deemed a promising hit through discernment of its potent *in vitro* activity judged by a minimum concentration to inhibit 90% of bacterial growth (MIC) of 150 nM, and acceptable Vero cell-based cytotoxicity as the concentration to inhibit the growth of Vero cells by 50% (CC₅₀) was 9.6 μM . JSF-2019 also exhibited a narrow spectrum of activity, with its only significant growth inhibition of the ESKAPE bacteria family observed with *Staphylococcus aureus* (ATCC 43300, MIC = 2.4 μM). JSF-2019 was bactericidal,

of action of these triazines, focusing primarily on JSF-2019 and the optimized analog JSF-2513 (Figure 1C), and demonstrated the significance of the intrabacterial F₄₂₀H₂-dependent release of nitric oxide (NO[•]) and the inhibition of the essential enoyl-acyl carrier protein reductase InhA. These results offer insights of value to the pursuit of next-generation nitro-containing antituberculars to supplant pretomanid and/or delamanid.

RESULTS

The Nitro Moiety Is Essential for Whole-Cell Activity

Analogues of JSF-2019 were prepared to assess the essentiality of the nitro moiety with respect to whole-cell efficacy (Table S1A). The des-nitro analog JSF-2026 was prepared via our general route to analogs of JSF-2019 that in this case specifically involved two sequential additions of aniline to cyanuric chloride and was followed by hydrazine addition and its capping with 5-nitrofuraldehyde (Figure 1D). As necessary for other syntheses

Table 1. MIC Values for Select Compounds versus Spontaneous *M. tuberculosis* JSF-2019-Resistant Mutant Strains

Strain	MIC (μ M)			Gene(s) Mutated (Amino Acid Change)
	JSF-2019	Pretomanid	INH	
Reference: H37Rv	0.078	0.039	0.16	–
2019_8x1	1.3	10	1.25	multiple mutations including <i>fbiB</i> (K208E) and <i>inhA</i> promoter (c(-15)t) ^a
2019_8x2	1.3	>40	0.16	<i>fgd1</i> (R283L)
2019_8x3	1.3	>40	0.16	<i>fgd1</i> (E205*)
2019_8x4	1.3	>40	0.16	<i>fgd1</i> (E205*)
2019_8x5	1.3	20	0.16	<i>fgd1</i> (G168*)
2019_8x6 [#]	0.63	5.0	0.16	<i>rv1435c</i> (A33S) <i>rv2623</i> (T84I)
2019_8x7 [#]	0.63	5.0	0.16	<i>rv2983</i> (D188N)
2019_8x8	1.3	>40	0.16	<i>fgd1</i> (E205*)
2019_8x9 [#]	0.63	5.0	0.16	<i>rv2983</i> (D188N)
2019_8x10 [#]	1.3	5.0	0.16	<i>ppnK</i> (V171M)
2019_16x1	1.3	>40	0.16	<i>fgd1</i> (E205*)
2019_16x2	1.3	>40	0.16	<i>fgd1</i> (E205*)
2019_16x3 [#]	1.3	10	0.16	<i>fbiB</i> (S54P) <i>ppnK</i> (V171M)
2019_16x4 [#]	1.3	5.0	0.16	<i>fbiB</i> (S54P) <i>ppnK</i> (V171M)
2019_16x5 [#]	2.5	2.5	0.16	<i>ppnK</i> (V234L) <i>rv2983</i> (C187*) <i>accA2</i> (A323T)
2019_16x6 [#]	1.3	5.0	0.16	<i>rv1435c</i> (A33S) <i>rv2632c</i> (T84I)
2019_16x7	1.3	>40	0.16	<i>fgd1</i> (E205*)

Mutated genes are listed with the amino acid change in parentheses. Mutations in strains marked with a hash mark (#) were identified by whole-genomic sequence while the others were identified by Sanger sequencing.

^aOther mutations observed were *rv2421c* (V54A), *snoP* (D151E), *rv1771* (Q291R), *rv1907c* (V158A), and *rv3058c* (D184H).

of analogs of JSF-2019, the order of addition of the various triazine substituents could be altered (Supplemental Information). JSF-2026 was 130-fold less active than JSF-2019, with significantly diminished whole-cell activity (MIC = 20 μ M). However, JSF-2026 was still more potent than des-nitro pretomanid, which was reported to lack quantifiable whole-cell efficacy (Singh et al., 2008). Replacement of the nitro moiety with electron-withdrawing groups (CF₃ in JSF-2389; CN in JSF-2390) also led to significant losses of activity.

Deficiency in the F₄₂₀H₂ Biosynthetic Pathway Leads to JSF-2019 Resistance

The early structure-activity relationship (SAR) as to the importance of the nitro group was reminiscent of pretomanid and delamanid and suggested a shared mode of bioactivation (Manjunatha et al., 2009; Singh et al., 2008). To probe this similarity, we raised *M. tuberculosis* spontaneous mutants resistant to

JSF-2019 in the H37Rv background. JSF-2019 exhibited a FOR of 1.3×10^{-6} at 8 \times MIC and 6.4×10^{-8} at 16 \times MIC. These FOR values are lower than those for pretomanid (10^{-5} – 10^{-6}) (Haver et al., 2015). Seventeen colonies were isolated and resistance was verified by MIC determination. JSF-2019 suffered a 16- to 64-fold loss of *in vitro* efficacy against all 17 strains (Table 1). We assayed for resistance of these 17 JSF-2019-resistant strains against pretomanid and the front-line drug isoniazid (INH), which inhibits the essential fatty acid biosynthetic enzyme *InhA* (Banerjee et al., 1994; Rozwarski et al., 1998; Vilcheze et al., 2006). All 17 strains exhibited resistance to pretomanid. Seven of 17 strains were highly resistant to pretomanid with a >1,000 \times shift in MIC (MIC >40 μ M), whereas 10 of 17 strains exhibited a 64–512 \times shift in MIC. Interestingly, 1 of 17 exhibited cross-resistance with INH, quantified by an 8 \times MIC shift versus the parental strain H37Rv.

It was reported that high-level resistant strains versus pretomanid harbored mutations within the F₄₂₀H₂ biosynthetic pathway (Haver et al., 2015), and we have previously reported low-level cross-resistance between JSF-2019 and pretomanid while investigating pyrimidine analogs (Inoyama et al., 2018). We, therefore, examined and confirmed that all seven mutants with high-level pretomanid cross-resistance possessed mutations in the *fgd1* open reading frame encoding F₄₂₀-dependent glucose-6-phosphate dehydrogenase via Sanger sequencing. Additionally, whole-genome sequencing identified two *fbiB* mutants and three *rv2983* mutants among ten strains with a moderate level of pretomanid cross-resistance. These genes encode two F₄₂₀ biosynthetic enzymes, converting FO into F₄₂₀ (Haver et al., 2015; Rifat et al., 2018). Finally, a transposon strain *fgd1::tn* in the H37Rv background demonstrated a 17-fold loss of susceptibility to JSF-2019 while only being 2-fold less susceptible to JSF-2026 (Table 2).

JSF-2019 Is an Intracellular NO[•] Donor Dependent on the Cofactor F₄₂₀H₂

We hypothesized that F₄₂₀-dependent activation of JSF-2019 was associated with NO[•] production and formation of a des-nitro metabolite (previously synthesized as JSF-2026) (Figure 2A). To test this hypothesis, we treated *M. tuberculosis* wild-type strain H37Rv and F₄₂₀H₂-deficient strain *fgd1::tn* with 20 μ M JSF-2019, using pretomanid and JSF-2026 as controls, and assayed for intracellular NO[•] quantification with the Griess reagent (Figures 2B and 2C) (Ding et al., 1988; Tan et al., 2010). Specifically, NO[•] released intracellularly due to compound activation would be oxidized and then effluxed from the cell into the media and quantified as nitrite NO₂[−]. During the 5-day exposure to an *M. tuberculosis* H37Rv culture, JSF-2019 generated a smaller yet quantifiable NO[•] release compared with pretomanid at an equimolar concentration (Figure 2B). This NO[•] release was not discernible in *fgd1::tn* cells, indicating that cofactor F₄₂₀H₂ was essential for JSF-2019 extrusion of NO[•] (Figure 2C). The nitro group in JSF-2019 was required for NO[•] release, as des-nitro JSF-2026 failed to generate NO[•] in either wild-type or *fgd1::tn* strains given the lower limit of quantification of 0.80 μ M NO₂[−].

We applied a liquid chromatography-mass spectrometry (LC-MS)-based intrabacterial drug metabolism (IBDM) assay to identify JSF-2019 metabolites inherent to NO[•] generation. Generally, a liquid culture of mid-log phase *M. tuberculosis*

Table 2. MIC Values for Select Compounds versus *M. tuberculosis* Strains with Mutations in *inhA*, *katG*, $F_{420}H_2$ Biosynthetic Genes, or *ddn*

Strain	Mutated Gene(s)	MIC (μ M)					
		JSF-2019	JSF-2026	JSF-2513	JSF-4328	Pretomanid	INH
H37Rv	\	0.078	20	0.63	>250	0.078	0.16
mc ² 4914	<i>inhA</i> promoter c(-15)t	0.63	20	2.5	>250	0.16	1.25
DRM12	<i>katG</i> (S315T)	0.078	20	0.63	ND	0.039	>10
<i>fgd1::tn</i>	<i>fgd1</i> transposon insertion	1.3	40	10	>250	>40	0.16
JSF- <i>Mtb</i> -1	<i>fbiC</i> F567S <i>inhA</i> promoter c(-15)t	5.0	40	20	>250	>40	1.25
<i>ddn::tn</i>	<i>ddn</i> transposon insertion	0.63	20	1.3	ND	>80	0.16

ND, not determined.

was subjected to compound treatment followed by metabolism quenching, metabolite extraction, and LC-MS analysis of the intrabacterial metabolites as a function of time. The IBDM protocol is based on previous methods for *M. tuberculosis* agar-based metabolomics developed by Rhee's group (Chakraborty et al., 2013) and a drug penetration assay reported by Dartois and colleagues (Sarathy et al., 2013). Our IBDM assay affords homogeneous compound exposure while attempting to minimize compound degradation during metabolite extraction. Here, we discuss its application to study the kinetics of intrabacterial metabolism of JSF-2019. *M. tuberculosis* H37Rv and *fgd1::tn* strains were treated with 20 μ M JSF-2019 for 24 h, followed by metabolite extraction and LC-MS interrogation. One peak with *m/z* of 372.1 amu [*M* + *H*⁺] was observed in the H37Rv lysate, consistent with des-nitro JSF-2026. LC-MS and high-resolution mass spectrometry (HRMS) confirmed that the observed des-nitro metabolite was identical to previously prepared JSF-2026 (Figure S1). This des-nitro metabolite was not detected when the *fgd1::tn* was cultured with JSF-2019 given the limit of detection of 1.2 pmol for JSF-2026 (Figure 2E). This indicated an $F_{420}H_2$ -dependent reductive metabolism of JSF-2019. Consistent with the previously established link between $F_{420}H_2$ and bio-reduction of the nitro moiety (Singh et al., 2008), sodium borohydride treatment of JSF-2019 led to formation of JSF-2026, as demonstrated by LC-MS. Consistent with its role as a product of nitro-group bioactivation, JSF-2026 suffered only a 2-fold shift in MIC versus the *fgd1* mutant strain as compared with the wild-type strain (Table 2).

We sought to correlate JSF-2019 metabolism with NO[•] release by studying the system kinetics in the H37Rv and *fgd1::tn* strains. These strains were treated with 20 μ M JSF-2019, after which nitrite levels were quantified in the supernatant while the metabolite profile of the pellet was probed by LC-MS at several time points. A rapid accumulation followed by a gradual decay of JSF-2019 was observed in H37Rv (Figure 2D). The des-nitro metabolite, JSF-2026, appeared after 4 h of treatment, which was concurrent with the formation of nitrite in the supernatant (Figures 2E and 2F). Metabolic transformation of JSF-2019 to produce JSF-2026 and NO[•] was not detectable in the $F_{420}H_2$ -deficient strain. The concurrent accumulation of nitrite and the des-nitro metabolite in H37Rv were indicative of an $F_{420}H_2$ -dependent metabolism resulting in NO[•] release. This $F_{420}H_2$ -dependent activation was further supported by the observed antagonism (at the 95% confidence interval, $-1.7 \leq$

$\kappa \leq -1.4$) between JSF-2019 and pretomanid in H37Rv quantified by BRAID analysis of the checkerboard assay (Twarog et al., 2016) (Figure S2A), compared with the lack of synergy or antagonism (at the 95% confidence interval, $-0.046 \leq \kappa \leq 0.51$) between INH and pretomanid (Figure S2B) and the weak synergy (at the 95% confidence interval, $0.12 \leq \kappa \leq 0.37$) between INH and JSF-2019 (Figure S2C). This antagonism was likely due to a competition for utilization of the $F_{420}H_2$ pool for activation between JSF-2019 and pretomanid.

Pretomanid has been reported to require activation by the nitroreductase Ddn utilizing $F_{420}H_2$ as a cofactor (Singh et al., 2008). The susceptibility of a *ddn* transposon insertion strain *ddn::tn* (Inoyama et al., 2018; Singh et al., 2008) to JSF-2019 and pretomanid was assessed (Table 2). As expected, functional inactivation of *ddn* afforded a >1,000-fold loss of susceptibility to pretomanid compared with the wild type. In contrast, JSF-2019 exhibited only an 8-fold loss of activity versus this transposon mutant compared with H37Rv, indicating that Ddn is not the primary nitroreductase activator for JSF-2019. As expected, JSF-2026 did not lose whole-cell efficacy versus the *ddn::tn* strain when compared with the wild type.

The Hydrazone Linker Is Optimal

Given SAR and mechanistic studies pointing to the importance of maintaining the nitrofurans of JSF-2019, we turned to the optimization of other aspects of the molecule (Table S1B), relying on the general synthetic route in Figure 1D. Methylation of the hydrazone N-H (cf. JSF-2113) was somewhat tolerated, as it led to an 8-fold loss in activity compared with JSF-2019. Methylation in combination with saturation of the hydrazone to afford hydrazine JSF-2116 did not result in a further loss of efficacy compared with JSF-2113. Replacement of the hydrazone with an acyl hydrazide (cf. JSF-2111) only afforded a 4-fold reduction in efficacy and did not significantly change Vero cell cytotoxicity. The alteration did significantly enhance solubility (*S* = 13.8 μ M versus <0.060 μ M for JSF-2019) while maintaining good mouse liver microsome (MLM) stability (*t*_{1/2} = 55.0 min versus 63.6 min for JSF-2019). *N*-methylation of this acyl hydrazide at N-1 (cf. JSF-2114) did not improve whole-cell activity, although it further increased Vero cell cytotoxicity. *N*-2 methylation (cf. JSF-2118) was not desirable, as it raised the MIC by a factor of 60. These limited investigations culminated with further profiling of JSF-2111, and a significant issue was noted with the compound's stability in mouse and

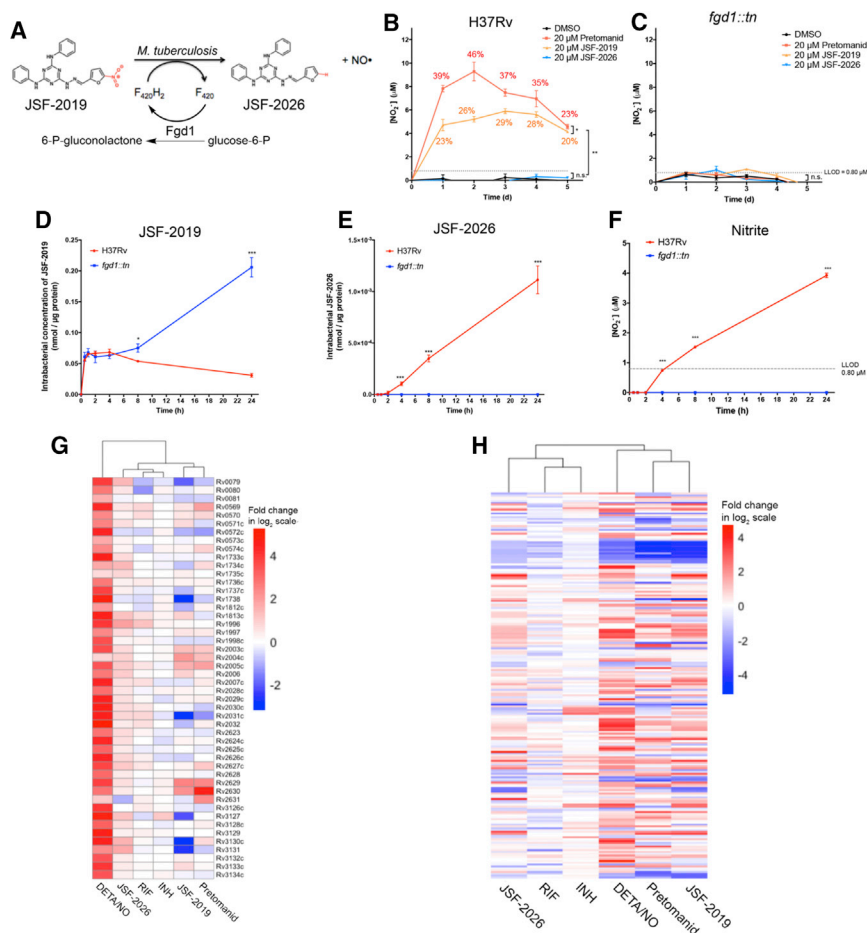


Figure 2. JSF-2019 Produces NO⁻ and JSF-2026 in a Process Dependent on F₄₂₀H₂

(A) Proposed scheme for JSF-2019 activation.

(B and C) *M. tuberculosis* strains H37Rv and *fgd1::tn*, respectively, were treated with 20 μM compound followed by nitrite quantification via the Griess reagent. Numbers above each data point indicate the molarity ratio of nitrite versus triazine dose. Gray dashed line indicates nitrite lower limit of detection (LLOD) as 0.80 μM. Data points are shown as mean ± standard error with three independent experiments. Statistical significance was analyzed by paired Student's t test. *p < 0.05; **p < 0.01; n.s., not statistically significant.

(D–F) H37Rv and *fgd1::tn* were treated with 20 μM JSF-2019 followed by study of the kinetics of intrabacterial metabolism and NO⁻ release. Data points are shown as mean ± standard error with three independent experiments. Statistical significance was analyzed by paired multiple t tests corrected for multiple comparison using the Holm-Sidak method. *p < 0.05; ***p < 0.001.

(G and H) Mid-log phase H37Rv were treated with 10x MIC of JSF-2019 and JSF-2026 followed by hierarchical analysis of transcriptional response comparison with INH, RIF (rifampicin), pretomanid, and DETA/NO (diethylenetriamine/nitric oxide adduct). (G) demonstrates responses in the *dosR* regulon and (H) shows responses in 212 NO⁻-sensitive non-*dosR* genes.

human plasma (68.4% and 63.8% compound remaining after 5 h of incubation, respectively; Table S2) compared with JSF-2019.

Enhanced Aqueous Solubility May Be Introduced through a Morpholine Substituent

Maintenance of the nitrofuryl hydrazone of JSF-2019 led us to explore replacement of both anilines with a wide range of amines. We contemplated the di-*i*-Pr analog of JSF-2019, shown to be *in vivo* active in 1969 (Bruhin et al., 1969). This compound was prepared and renamed as JSF-2032, and exhibited diminished whole-cell activity (MIC = 1.4 μM), although in a model of intracellular infection with mc²6206-infected J774.1 cells (Kumar et al., 2018), its IC₅₀ (minimum compound concentration to inhibit bacterial growth by 50%) versus mc²6206-infected J774.1 cells was slightly better than that of JSF-2019 (0.13 versus 0.27 μM) with INH (IC₅₀ = 0.44 μM) and rifampicin (RIF) (IC₅₀ = 0.13 μM) as positive controls. JSF-2032 exhibited decreased MLM stability (*t*_{1/2} = 31.8 min) compared with JSF-2019, but it was judged significant that its solubility (*S* = 27.5 μM) was much improved versus JSF-2019. Interestingly, the mouse 5-h PK study (two mice, one 25 mg/kg oral dose with 5% dimethylacetamide [DMA]/60% polyethylene glycol 300/35% D5W [5% dextrose in water] as the formulation, unless noted otherwise) for JSF-2032 demon-

strated no time above the MIC (*t* > MIC) and a reduction in compound exposure in the plasma, as quantified by AUC, compared with JSF-2019 (1,082 versus 1,148 h*ng/mL). Following an approach of exchanging both anilines in JSF-2019 with the same amine and utilizing the synthetic chemistry shown in Figure 1D, we explored a range of cyclic and acyclic amines (Table S1C). While solely considering MIC and Vero cell CC₅₀ values, we identified promising substitutions to be cyclopropyl (cf. JSF-2377), cyclobutyl (cf. JSF-2378), 4-F-cyclobutyl (cf. JSF-2592), cyclobutylmethyl (cf. JSF-2511), cyclopentyl (cf. JSF-2379), and cyclohexyl (cf. JSF-2380). Some variation in Vero cell cytotoxicity was noted in this series. *N*-methylation of each of the secondary amines in this group was not explored, although it may be noted that the bis(di-cyclobutylamino) analog (cf. JSF-2594) was active (MIC = 0.81 μM). This, however, represented a loss in activity compared with the mono-cyclobutyl JSF-2378 (MIC = 0.11 μM). Cyclic amines such as azetidine (cf. JSF-2589) and thiomorpholine (cf. JSF-2343) were slightly less active than JSF-2019. A noteworthy compound in this series was bis(morpholine) JSF-2189. Although it was less active than JSF-2019 with an MIC = 7.8 μM, it displayed promising solubility (*S* = 20.2 μM) and MLM stability (*t*_{1/2} = 68.0 min).

Mono(amine) Mono(morpholine) Analogs Show Promising Initial Profiles

To enhance the potency of JSF-2189, we leveraged the learnings with the other di(alkylamino) triazines discussed

Table 3. Mouse PK Comparison among Select Triazines

	JSF-2019	JSF-2513	JSF-2619	JSF-2625
AUC _{0-5h} ^a (h*ng/mL)	1148	12,025	7639	538
C _{max} ^a (ng/mL)	317	1707	4200	266
AUC _{0-5h} /MIC ^a	14	120	19	5.5
C _{max} /MIC ^a	5.1	18	11	2.7
<i>t</i> > MIC ^a (h)	5.0	8–24	3–5	1–3
C _{lung} /C _{plasma} at 5 h	2.6	BLQ	0.23	0.30
%F	ND	≥ 99	49.2	11.4
<i>t</i> _{1/2} (h) ^b	ND	0.43	0.36	0.19
Clearance (mL/(kg*h)) ^b	ND	2232	3700	5283
V _d (L/kg) ^b	ND	1.38	1.91	1.44

BLQ, below level of quantification; ND, not determined.

^aFollowing administration of a single 25-mg/kg oral dose.^bFollowing administration of a single 5-mg/kg intravenous dose.

above and the synthetic route in Figure 1D, and explored the replacement of one of the two morpholines with a primary or secondary amine (Table S1D). Acyclic and cyclic alkyl amines were examined in this subseries. Among the acyclic amines, *i*-propyl amine JSF-2621 exhibited the most preferable combination of properties, most prominently with an MIC = 0.13 μ M, Vero cell CC₅₀ = 130 μ M, S = 25.4 μ M, and MLM *t*_{1/2} = 54.2 min. Homologation of the alkyl moiety (cf. JSF-2595), methylation of the amine nitrogen (cf. JSF-2683), and replacement of the methine hydrogen with a methyl group (cf. JSF-3382) all led to a loss of whole-cell activity (4- to 15-fold). Cyclization of the one amine substituent was then investigated with pendant 3- to 5-membered rings. Cyclopropylamine JSF-2624 and α -methylcyclopropylamine JSF-2625 exhibited the most promising profiles. It was interesting to observe that while both compounds were similar in potency (MIC = 0.26 and 0.25 μ M, respectively) their solubility (S = 117 and 8.71 μ M, respectively) and MLM stability (*t*_{1/2} = 22.0 and 56.4 min, respectively) values differed substantially based on the α -methyl substitution. *N*-methylation (cf. JSF-2684) or homologation (cf. JSF-2686 or JSF-2786) of JSF-2624 led to slight losses in activity and significant increases in Vero cell cytotoxicity. The corresponding cyclobutyl series (cf. JSF-2682, -2620, -2685, -2707, -2706, -2705) and cyclopentyl (cf. JSF-3249, -3366) subseries did not offer considerable advantages over the cyclopropyl analogs. Secondary amines were also examined with azetidines JSF-2619 proving superior to pyrrolidines JSF-2886. Aromatic amines were examined, beginning with aniline JSF-2513, which demonstrated a promising MIC of 0.63 μ M and S = 0.853 μ M, and modest Vero cell CC₅₀ of 3.9 μ M. Introduction of a methyl, fluoro, cyano, or methoxy group at the 2-, 3-, or 4-positions (cf. JSF-2804, -2805, -2807, -2835–7, -2884, -2888, -2923, -2892, -2890, -2894, -2895) failed to enhance the MIC but did improve the Vero cell CC₅₀. Homologation to the corresponding benzylamine (with or without mono- or dimethylation of the benzylic carbon) afforded compounds (cf. JSF-3546, -3401–3403) with an MIC > 1 μ M. Methyl- or chloro-substituted benzyl analogs (cf. JSF-3457, -3458, -3585, -3474, -3586, -3473) were similarly unremarkable. Replacement of the benzene ring in benzyl analog

JSF-3456 with furan (cf. JSF-3511), thiophene (cf. JSF-3510), thiazole (cf. JSF-3543), pyridine (cf. JSF-3524), pyrimidine (cf. JSF-3542), and pyrazine (cf. JSF-3541) also did not improve upon the MIC of JSF-2513.

Further Profiling of Select Analogs Leads to JSF-2513 as an *In Vivo* Efficacy Candidate

A comparison of MIC, Vero cell CC₅₀, S, and MLM *t*_{1/2} values led to the selection of JSF-2513, JSF-2619, and JSF-2625 for further profiling. Each compound was assessed for 24-h PK profile (Table 3) in three mice dosed with 25 mg/kg orally with a 0.5% carboxymethylcellulose (CMC)/0.5% Tween 80 formulation and in three mice dosed 5 mg/kg intravenously with a 5% DMA/95% (4% cremophor in 0.9% saline) formulation. A comparison of the three compounds (Tables S1 and S3; Figures S3A–S3C) favored JSF-2513 over JSF-2625 and JSF-2619 due to its AUC, *t* > MIC, and oral bioavailability (%F) metrics. The corresponding values for JSF-2625 were surprisingly low and warranted further investigation. JSF-2625 in mouse plasma, aqueous dimethyl sulfoxide, or aqueous CH₃CN was found to degrade through a presumptive C–N bond cleavage reaction to afford aminotriazine JSF-3226 (Figure S4). JSF-3226 was synthesized independently, via adaptation of the route in Figure 1D, and demonstrated via ¹H nuclear magnetic resonance and LC–MS characterization to be identical to the degradant isolated from aqueous acetonitrile. JSF-3226 was found to be significantly less active than *M. tuberculosis* (MIC = 3.9 μ M). This decomposition process was light dependent and was most apparent in triazines containing an alkylamine substituent. JSF-2513 and JSF-2619 were not found to be as vulnerable to this cleavage reaction and demonstrated satisfactory stabilities in mouse plasma (Table S2).

With the data package weighing in favor of JSF-2513, further *in vitro* activity profiling was conducted. The antitubercular activity of JSF-2513 was dependent on F₄₂₀H₂ cofactor, judged by a 16-fold potency loss versus the *fgd1::tn* strain, but not significantly on a functional Ddn, as its MIC only increased 2-fold against the *ddn::tn* strain (Table 2). JSF-2513 generated NO[•] in the *M. tuberculosis* H37Rv strain in a lesser amount than JSF-2019 at equimolar concentrations, and this NO[•] release was abolished in *fgd1::tn* cells (Figures 3A–3C). The F₄₂₀H₂-dependent nitro-group activation of JSF-2513 produced the des-nitro metabolite JSF-4328 (Figures 3A and S5), in analogy to JSF-2026 derivation from JSF-2019.

JSF-2513 exhibited MIC values in excess of 120 μ M versus strains of *Klebsiella pneumoniae*, *Acinetobacter baumannii*, *Pseudomonas aeruginosa*, and *Enterobacter cloacae*, while showing modest *in vitro* activity against *Enterococcus faecium* (MIC = 15 μ M) and *S. aureus* (MIC = 29 μ M). The MBC of JSF-2513 was determined to be 1.6 μ M. JSF-2513 exhibited an IC₅₀ value of 1.3 μ M versus mc²6206-infected J774.1 cells. In the Hu-Coates model of non-replicating persistence that probes compound cidal activity versus 100-day-old cultures of *M. tuberculosis* (Hu et al., 2003), at a 100- μ M concentration JSF-2513 and JSF-2019 afforded ca. 7 and 4 log₁₀ reductions in colony-forming units (CFUs), respectively, as compared with 6 log₁₀ for pretomanid (Figure S3E).

Profiling of the mouse and human plasma protein binding of JSF-2513 (Table S2) was conducted. JSF-2513 exhibited high,

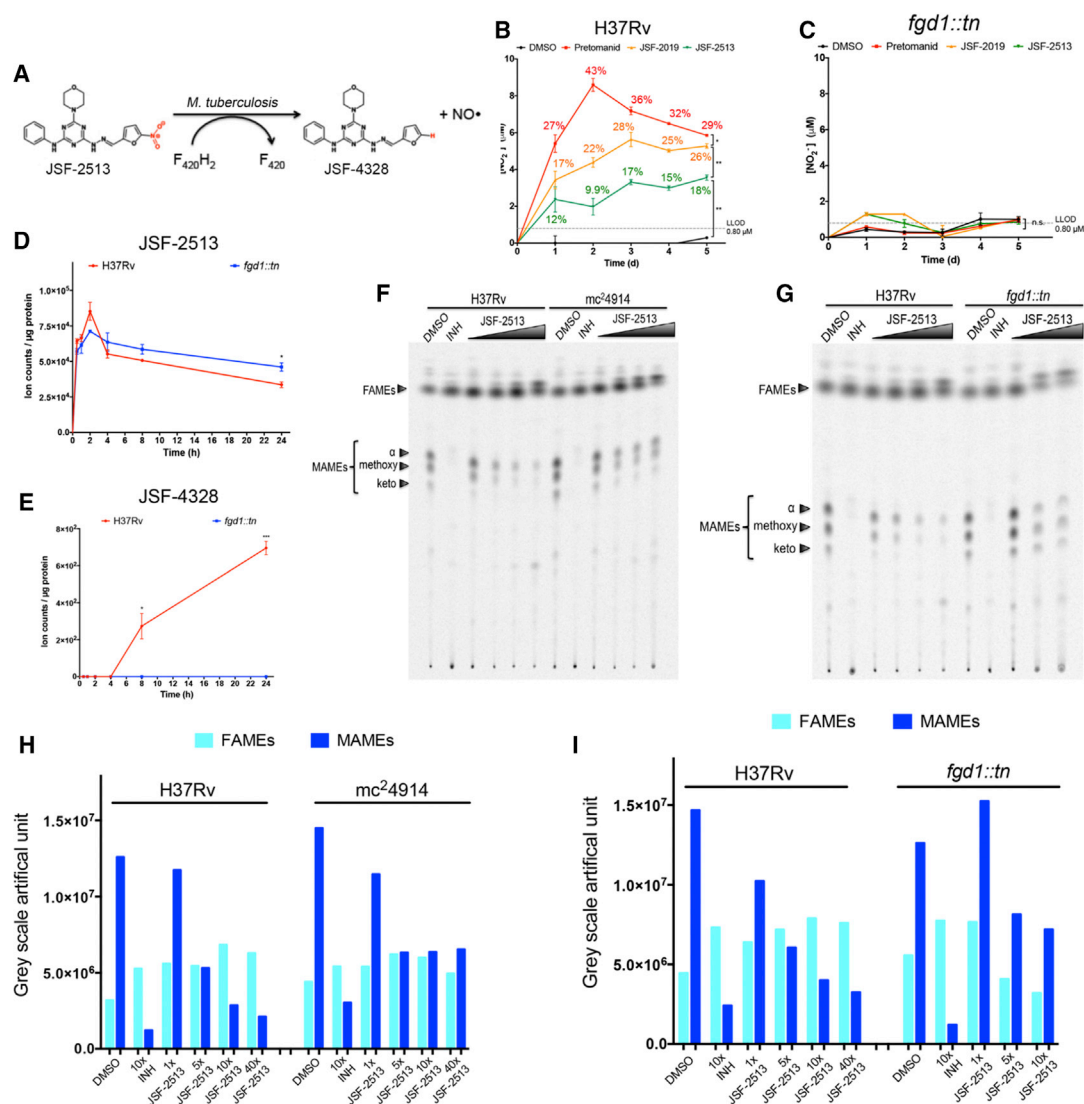


Figure 3. JSF-2513 Intrabacterial Metabolism Releases NO^+ with JSF-4328 Formation and FAS-II Inhibition

(A) Proposed scheme for JSF-2513 activation.

(B and C) *M. tuberculosis* strains H37Rv and *fgd1::tn* were treated with 20 μM compound followed by nitrite quantification by Griess reagent. Numbers above each data point indicate the molarity ratio of nitrite versus triazine dose. Gray dashed line indicates nitrite lower limit of detection (LLOD) as 0.80 μM . Data points are shown as mean \pm standard error with three independent experiments. Statistical significance was analyzed by paired Student's *t* test. **p* < 0.05; ***p* < 0.01; n.s., not statistically significant.

(D and E) H37Rv and *fgd1::tn* were treated with 20 μM JSF-2513 and the time courses for intrabacterial metabolism (JSF-4328 formation) and NO^+ release were followed. Data points were shown as mean \pm standard error with three independent experiments. Statistical significance was analyzed by paired multiple *t* tests corrected for multiple comparison using the Holm-Sidak method. **p* < 0.05; ****p* < 0.001.

(F and G) *M. tuberculosis* strains H37Rv, *mc*²4914, and *fgd1::tn* were treated with 10x MIC of JSF-2513 or INH, as a control, for 8 h and assessed for [¹⁴C]acetate labeling after 16 h. FAMES and MAMES were extracted and analyzed via TLC. Dose of JSF-2513 in H37Rv: 1x (0.63 μM), 5x, 10x, and 40x MIC. Dose of JSF-2513 in *mc*²4914: 1x (2.5 μM), 5x, 10x, and 40x. Dose of JSF-2513 in *fgd1::tn*: 1x (10 μM), 5x, and 10x. INH was at 10x MIC.

(H and I) Grayscale densitometric analysis of MAMES and FAMES from (F) and (G), respectively, using ImageJ.

but still acceptable, binding to plasma proteins from mouse (99.0%) and human (98.0%). Finally, JSF-2513 exhibited acceptable human liver microsomal stability ($t_{1/2}$ = 61.7 min; Cl_{int} = 11.2 $\mu L/min/mg$ protein) and did not significantly inhibit human cytochrome P450 isoforms (Table S3). Complete mouse PK profiling for JSF-2513 required testing dose proportionality and tolerability in mice (Figure S3D) at single doses of 50 to

300 mg/kg. Dosing of JSF-2513 at 300 mg/kg resulted in lethargy in the mice. The level of JSF-2513 in the mouse lungs was near the limit of quantification (25 ng/mL) 5 h after a single 25-mg/kg dose. Similar experiments with 60- and 200-mg/kg dosing enabled more accurate determination of this parameter. JSF-2513 achieved lung/plasma concentration ratios of 0.55 and 0.67 at 60- and 200-mg/kg dosing, respectively. These

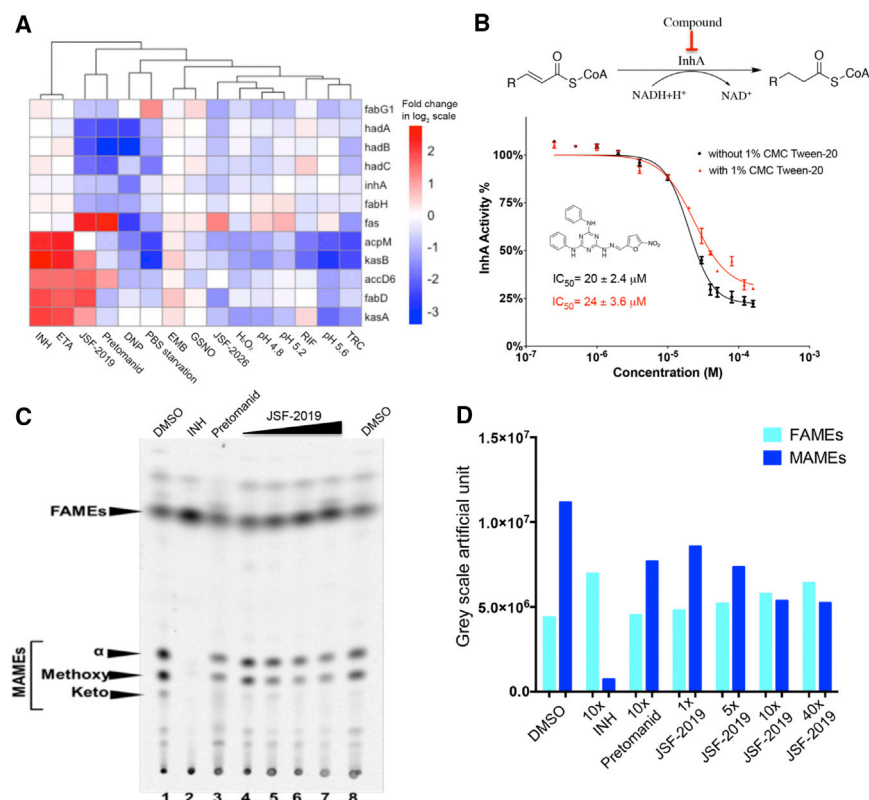


Figure 4. JSF-2019 Is an InhA Inhibitor

(A) Mid-log phase *M. tuberculosis* cultures were treated with 10× MIC of JSF-2019 or JSF-2026 for 6 h, followed by mRNA extraction and RNA-seq analysis. Hierarchical clustering analysis with Euclidean distance was applied to the gene-expression profiles to compare transcriptional responses in FAS-II genes induced by JSF-2019 or JSF-2026 to responses generated by other stress conditions. RIF, rifampicin; INH, isoniazid; ETA, ethionamide; DNP, 2,4-dinitrophenol; EMB, ethambutol; GSNO, S-nitrosoglutathione; TRC, triclosan.

(B) The InhA *in vitro* enzyme assay scheme is depicted. JSF-2019 IC₅₀ for InhA inhibition was quantified with and without 1% CMC Tween 20. Each data point is shown as mean ± standard error, and IC₅₀ was determined via non-linear regression model.

(C) FAS TLC for *M. tuberculosis* H37Rv treated with JSF-2019 at 1×, 5×, 10×, and 40× MIC for 4 h, with INH at 10× MIC and pretomanid at 10× MIC as controls.

(D) Grayscale densitometric analysis of MAMES and FAMES from (C) using ImageJ.

values were in our acceptable range of 0.5–1.0 and comparable with other profiled analogs, but were less than those determined for JSF-2019 and JSF-2032 (Table S4). To sum up, the total of PK studies supported 60 and 200 mg/kg as the dosing levels for an acute infection model (Rao et al., 2013). JSF-2513 and INH, as a positive control at 25 mg/kg, were compared with vehicle alone in dosed Balb/c mice at their selected levels beginning 2 weeks post infection ($t = 0$), and the bacterial burden was quantified via the lung CFUs at selected time points. After 4 weeks of dosing, JSF-2513 failed to demonstrate a reduction in *M. tuberculosis* CFUs in mouse lungs and spleen as compared with the vehicle alone.

The Transcriptional Profile of JSF-2019 Supports NO⁺ Release and FAS-II Inhibition

While plotting a strategy to further optimize the triazine series for *in vivo* efficacy, we had the opportunity to further probe the mechanism of action of JSF-2019 as to better inform future optimizations. The transcriptional response of *M. tuberculosis* H37Rv cultures treated with 10× MIC of JSF-2019 or des-nitro compound JSF-2026 were quantified by RNA sequencing (RNA-seq) and analyzed via hierarchical clustering (Data S1) (Boshoff et al., 2004). The expression profiles of NO⁺-responsive genes, including the *dosR* regulon and non-*dosR* genes, were examined and compared with previously published microarray data for diethylenetriamine/nitric oxide adduct (DETA/NO) and pretomanid (Voskuil et al., 2011). DETA/NO, an extracellular NO⁺ donor, strongly induced the *dosR* regulon as previously reported. This *dosR* regulon upregulation was specific for extracellular nitric oxide stress, in contrast to profiles for

with differing mechanisms of action (Figure 2G). Voskuil et al. (2011) reported 212 non-*dosR* genes that were sensitive to reactive nitrogen species. Nitric oxide stress, regardless of the intracellular or extracellular donors of NO⁺, specifically and significantly differentiated expression of these 212 genes in comparison with treatments with INH, RIF, or des-nitro JSF-2026 (Figure 2H).

Given that pretomanid has also been reported to affect mycolic acid biosynthesis by depleting keto mycolates (Stover et al., 2000), we probed the effect of JSF-2019 on *M. tuberculosis* fatty acid biosynthesis (FAS) gene transcript levels. JSF-2019 treatment of *M. tuberculosis* resulted in a FAS expression profile similar to that of pretomanid according to hierarchical clustering analysis, primarily due to the downregulation of several FAS-II genes (*hadABC*, *inhA*, and *fabH*) (Figure 4A). In contrast to JSF-2019, des-nitro JSF-2026 did not significantly alter FAS-II gene expression with respect to the criteria fold change >2 and false discovery rate p value <0.05. Therefore, it was suggested that mycolic acid biosynthesis may be responsive to NO⁺ stress. Downregulation of several FAS-II genes in the presence of NO⁺ was not observed in the expression profile of *M. tuberculosis* treated with FAS-II enzyme inhibitors such as INH and ethionamide (ETH). Intriguingly, some FAS-II genes, such as *kasA*, *kasB*, *acpM*, and *accD6*, were induced by JSF-2019 treatment, which was reminiscent of a typical FAS-II inhibition profile as mediated by INH or ETH (Wilson et al., 1999). Since this response has not been observed with pretomanid treatment (Manjunatha et al., 2009; Stover et al., 2000), we hypothesized that JSF-2019 may kill *M. tuberculosis* through FAS-II inhibition as well as NO⁺ release.

JSF-2019 Inhibits InhA

Given our lab's experience with InhA (Freundlich et al., 2009; Stec et al., 2014; Vilcheze et al., 2011), we began by probing the interaction of JSF-2019 with InhA. JSF-2019 inhibited ($IC_{50} = 20 \pm 2.4 \mu M$) the functional activity of purified InhA, as quantified by the reduction of the model substrate 2-dodecenoil-coenzyme A in the presence of NADH (Figure 4B). We further assayed for InhA inhibition by JSF-2019 in the presence of added detergent. JSF-2019 demonstrated an $IC_{50} = 24 \pm 3.6 \mu M$ in the presence of 1% CMC Tween 20 (Figure 4B). This minimal IC_{50} shift supported JSF-2019 as a modest InhA inhibitor *in vitro* and ruled out promiscuous enzyme inhibition through the formation of aggregates (Feng and Shoichet, 2006; Feng et al., 2007; Shoichet, 2006). This modest enzyme inhibition was slightly depressed (43%–26%) when the hydrazine linker in JSF-2019 was modified via methylation, substitution to the corresponding hydrazide with or without *N*-methylation, or reduction to the hydrazine with or without *N*-methylation (Table S1B). It should be noted that significant efforts to obtain an X-ray crystal structure of InhA with bound JSF-2019 were unsuccessful (unpublished data). The shared inhibition of InhA and the commonality of the hydrazine (-NHNH-) fragment between JSF-2019 and INH hinted at a role for the catalase-peroxidase KatG (Rozwarski et al., 1998; Zhang et al., 1992) in the intrabacterial activation of JSF-2019. However, KatG does not appear to have a significant effect on the activity of JSF-2019 (or JSF-2026 or JSF-2513) within *M. tuberculosis* given the lack of an MIC shift as compared with the wild-type H37Rv strain, versus a laboratory strain (DRM12) (Kumar et al., 2018) with the KatG S315T mutation that affords a >62-fold loss of efficacy for INH (Table 2). Additionally, JSF-2019 maintained its wild-type strain activity versus three strains (TDR31, TDR36, and TDR116) in our collection of drug-resistant clinical isolates from the Special Program for Research and Training in Tropical Diseases established by UNICEF/UNDP/World Bank/WHO Special Programs with the KatG S315T mutation (Kumar et al., 2018).

We questioned whether this modulation of the catalytic activity of InhA occurred within the bacterium. *M. tuberculosis* H37Rv was treated with increasing doses of JSF-2019 followed by labeling of the cultures with [^{14}C]acetate. As an InhA inhibitor, INH at 10 \times MIC afforded the expected FAS-II inhibition profile as judged by thin-layer chromatography (TLC) (Figures 4C and 4D): reduction of mycolic acids (visualized as mycolic acid methyl esters [MAMES] as per the protocol) accompanied by an accumulation of upstream short-chain fatty acids (visualized as short-chain fatty acid methyl esters [FAMES]) (Slayden and Barry, 2001; Wilson et al., 2013). In contrast, pretomanid treatment at 10 \times MIC led to a decrease of MAMES, purportedly resulting from the downstream effect/s of NO $^+$ release. JSF-2019 treatment, ranging from 1 \times to 40 \times MIC, resulted in the accumulation of FAMES and decrease of MAMES, consistent with FAS-II inhibition. This JSF-2019-mediated mycolic acid inhibition was diminished in an *inhA* overexpression strain (mc 2 4914) (Vilcheze et al., 2006) (Figure S6), further supporting JSF-2019 as an InhA inhibitor within the bacterium. It was intriguing to note that mycolic acid inhibition was also mitigated in the *fgd1::tn* strain, suggesting that a metabolite of JSF-2019, other than JSF-2026 which does not exhibit significant inhibi-

tion of purified InhA (its inhibition was abrogated in the 1% CMC Tween 20) (Figure S7A) or perturb mycolic acid biosynthesis in H37Rv as seen by TLC (Figures S6C and S6D), could also play a role in FAS-II inhibition.

We further confirmed JSF-2019 as an InhA inhibitor by assessing its efficacy versus an *M. tuberculosis* strain mc 2 4914 overexpressing *inhA* (Table 2). InhA overexpression in mc 2 4914 led to an 8-fold loss of activity for JSF-2019 or the positive control INH compared with the wild-type H37Rv strain. Further supporting the negligible role of metabolite JSF-2026 as an InhA inhibitor was its lack of an MIC shift between these strains. JSF-2019 showed reduced efficacy versus an *fgd1::tn* strain, as judged by a 17-fold MIC shift compared with the H37Rv strain. JSF-2019 exhibited a larger MIC change (64 \times) in strain JSF-*Mtb*-1, which featured both an F $_{420H_2}$ deficiency (F567S mutation in FbiC) in addition to *inhA* overexpression (*inhA* promoter c(-15)t) as seen with mc 2 4914. This susceptibility profiling supported a dual mechanism of action of JSF-2019 that is pertinent to NO $^+$ release and InhA inhibition.

Evidence Suggests that a JSF-2513 Metabolite Inhibits InhA, and More Generally FAS-II, in *M. tuberculosis*

JSF-2513 displayed a 4-fold MIC shift against the *inhA* overexpression strain mc 2 4914 compared with the H37Rv strain (Table 2), supportive of its InhA inhibition within the bacterium. Mycolic acid biosynthesis inhibition within the bacterium was further indicated by a TLC FAS-II inhibition pattern, judged by depletion of MAMES and accumulation of precursor FAMES in a JSF-2513 dose-dependent manner (Figures 3F and 3H). Overexpression of *inhA* in the mc 2 4914 strain mitigated FAS-II inhibition by JSF-2513 compared with the H37Rv strain. However, JSF-2513 failed to demonstrate even modest inhibition of purified InhA in the enzyme assay with an $IC_{50} > 150 \mu M$ (Figure S7B). Following a suspicion that the intrabacterial FAS-II inhibition may derive from the action of a metabolite of JSF-2513, we tested the JSF-2513 inhibition of mycolate biosynthesis in the *fgd1::tn* strain, in which JSF-2513 intrabacterial metabolism was reduced as compared with the H37Rv strain (Figures 3C and 3D). JSF-2513 FAS-II inhibition, as judged by FAMES and MAMES (Figures 3G and 3I), was decreased in the *fgd1::tn* strain as compared with the H37Rv strain, suggesting a correlation between F $_{420H_2}$ -associated intrabacterial metabolism of JSF-2513 and its InhA and, more generally, FAS-II inhibition. The inhibition does not appear to involve the des-nitro metabolite JSF-4328, as the independently synthesized compound did not exhibit significant inhibition of purified InhA (29% \pm 0.79% inhibition at 50 μM compound in the presence of 1% CMC Tween 20), and its MIC was quantified as >250 μM versus the H37Rv, mc 2 4914, *fgd1::tn*, and JSF-*Mtb*-1 strains (Table 2).

NO $^+$ Release Drives Antitubercular Activity among a Subset of Triazines

To further understand the relative contributions of InhA inhibition and NO $^+$ release to whole-cell activity, we examined the activity profiles of eight triazines, including JSF-2019 and JSF-2513, and also pretomanid (Table S5). The selected triazines exhibited either potent (MIC < 1 μM) or moderate (1 < MIC < 10 μM) anti-tubercular activities versus H37Rv. The amount of NO $^+$ release

in H37Rv was measured over 4 days and quantified by an AUC_{0-4d} for all eight triazines. These analogs lose 4- to 64-fold *in vitro* activity against the *fgd1::tn* strain as compared with H37Rv. The potency of InhA inhibition was assessed via the percent inhibition of purified InhA by a 50 μ M concentration of each compound in the presence of 1% CMC Tween 20 to obviate any aggregation effects, with pretomanid serving as a negative control. A graphical analysis, though limited by a small sample size, demonstrated a curvilinear relationship between MIC and NO^+ AUC_{0-4d} (Figure S7C), indicating that increasing bacterial growth inhibition correlated with increasing NO^+ production. The data also suggested a lack of a significant relationship between MIC and percent InhA inhibition (Figure S7D). This latter observation stands in contrast to the MIC shift of 2- to 8-fold for these analogs when *inhA* was overexpressed (MIC values with mc²4914 versus H37Rv).

DISCUSSION

The clinical need for a next generation of antitubercular agents is driving chemical biology and medicinal chemistry efforts to explore novel chemotypes and mechanisms of action. We have herein detailed efforts with a triazine series, rediscovered through our efforts with machine learning models (Ekins et al., 2013). The series exhibited the potential to move beyond issues with other nitro-containing compounds of clinical relevance (pretomanid and delamanid). In particular, JSF-2019 displayed a lower frequency of resistance and a significantly reduced loss of *in vitro* efficacy versus these drug-resistant strains compared with pretomanid. The optimization focused on parameters known to be relevant to compound PK profile in mice, which in turn influences *in vivo* efficacy. Managing a multi-criteria optimization (MIC, CC₅₀, S, MLM $t_{1/2}$, mouse PK AUC, and $t > MIC$) and also navigating a chemical stability issue with alkylaminotriazines led us to JSF-2513. Along the way the importance of the morpholine substituent in modulating compound solubility, and hence PK, was recognized, reaffirming the utility of this family of heterocycles (Allison et al., 2006; Brickner et al., 1996; Frohlich and Tsogoeva, 2016; Scott et al., 2012; Summa et al., 2006). Despite this effort, JSF-2513 did not demonstrate significant efficacy in the mouse model of acute infection.

Aiding the continued optimization of these triazines will be the knowledge gained regarding their mechanism of action. These compounds are noted to contain a nitrofuran, leading to the supposition that their activity resides primarily in their ability to release NO^+ similar to pretomanid and delamanid. This hypothesis has been proved correct, as JSF-2019 and JSF-2513 both release NO^+ in a time-dependent fashion and the quantity of NO^+ release correlated significantly with antitubercular MIC. NO^+ release has been demonstrated to be cidal to *M. tuberculosis* whether occurring within the bacterium, via the bioactivation of pretomanid (Singh et al., 2008) or delamanid (Hoffmann et al., 2016; Matsumoto et al., 2006), or within the context of an intracellular infection (MacMicking et al., 1997). It is interesting to note that the respective NO^+ release efficiencies of JSF-2019 and JSF-2513 were less than that of pretomanid. Through resistant mutant studies, the activation of JSF-2019 appeared to share with pretomanid and delamanid the requirement for $F_{420}H_2$. How-

ever, the significantly smaller losses of whole-cell efficacy of JSF-2019, as compared with pretomanid, versus *M. tuberculosis* strains harboring mutations in *fgd1*, *fbtB*, or *fbtC* suggest differences in their respective activations. Additionally, the large differential in their MIC shifts against the transposon mutagenized *ddn* strain evidenced that while pretomanid primarily relies on reduction by the nitroreductase Ddn, JSF-2019 may require one or more other nitroreductases to release NO^+ . Other nitroreductases with significant sequence homology to Ddn include Rv1261c (Gurumurthy et al., 2013), Rv1558, and Rv3178 (Singh et al., 2008). They have been suggested as activating enzymes for analogs of pretomanid and its parent CGI-17341 (Gurumurthy et al., 2012). While the assay of Rv1261c and Rv1558 with regard to the activation of nitroheterocycles has not been reported, they and Ddn have been demonstrated to share quinone reductase activity (Gurumurthy et al., 2013). Although significantly different in sequence from the above nitroreductases, Rv2466c has been reported by two groups (Albesa-Jove et al., 2014; Negri et al., 2018; Rosado et al., 2017) to be a mycothiol-dependent nitroreductase. Finally, Rv2032, Rv3131, and Rv3127 have been hypothesized as nitroreductases due to their sequence similarity to annotated nitroreductases from other bacteria. *rv2032* appears to be co-regulated with *acr* under multiple stress conditions including intracellular infection (Purkayastha et al., 2002) and is essential for survival in macrophages and infected mice (Hu and Coates, 2011). However, Hu and Coates (2011) provided data that question the ability of Rv2032 to function as a nitroreductase and activate nitro-containing compounds such as nitro-furan and nitrofurantoin. Clearly, much more is to be learned about these proteins with regard to their native function and involvement in the bioactivation of nitro-containing antitubercular agents. The potential exists to leverage our developing understanding of multiple nitro-group reducing systems to rationally develop antituberculars of clinical significance that avoid the drug-resistance liabilities (both frequency of resistance and extent of loss of efficacy) of pretomanid and delamanid.

The metabolic lability of JSF-2019 and JSF-2513, due at least in part to nitro-group activation, highlights the importance of probing the intrabacterial metabolism of antituberculars. Small-molecule inhibitors should not be considered to always be inert within the bacterium; they may suffer intrabacterial metabolism, including but not limited to hydrolysis, *N*-alkylation, amidation, and, most relevant to this work, nitro-group activation (Awasthi and Freundlich, 2017). With our IBDM assay, we were able to reveal conversion of JSF-2019 and JSF-2513 to their respective des-nitro metabolites and study the metabolism kinetics. JSF-2019 accumulation was greater in nitro-group metabolism-deficient strains (e.g., *fgd1::tn*) than in the H37Rv strain. Correspondingly, an increase in JSF-2019 level was accompanied by decreases in the des-nitro metabolite (JSF-2026) and in NO^+ release as measured by the Griess assay. At the same time, it is important to acknowledge that we cannot discount the IBDM of JSF-2019 to provide other yet to be identified metabolites with a crucial role in mechanism of action. The decrease in the FAS-II inhibitory activity of JSF-2019 in the *fgd1::tn* strain, as seen via TLC, suggests the potential role of other metabolites (including NO^+) to inhibit InhA and/or other steps in fatty acid biosynthesis. This is consistent with our study of a subset of JSF-2019 analogs, including JSF-2513, where the *in vitro* growth

inhibition increased with the amount of NO⁺ release. However, the *in vitro* growth inhibition did not necessarily increase with the extent of inhibition of purified InhA, measured in the absence of the cell. This is despite an observed MIC increase when comparing each JSF-2019 analog's efficacy against the mc²4914 strain as compared with the H37Rv strain. An explanation may be found in the potential for one or more metabolites of each of these analogs to inhibit InhA within the bacterium. We also cannot discount the inhibition of other FAS-II enzymes that would contribute to the observed TLC profile (MAMEs reduction and FAMEs increase) for treated H37Rv. We assert that the IBDM platform is positioned to make significant contributions to these future mechanistic studies. Overall, the inhibition of InhA by these triazines (and/or their metabolites) differentiates them from pretomanid and delamanid and offers a promising therapeutic strategy when considered in concert with NO⁺ release.

SIGNIFICANCE

The nitro-containing antitubercular clinical compounds, delamanid and pretomanid, do not appear to be ideal additions to tuberculosis chemotherapy. In an effort to affect next-generation compounds, we have presented studies on the triazine JSF-2019 and its analogs. Optimization efforts detailed herein emphasize the utility of a morpholine moiety, present in evolved compounds such as JSF-2513, to improve compound solubility and mouse plasma PK. Mechanistic studies have relied on an intrabacterial drug metabolism platform that has detailed the activation of select triazines and its link to NO⁺ production. JSF-2019 is distinct from delamanid and pretomanid in that its efficacy is dependent on both NO⁺ release and InhA inhibition. The intrabacterial metabolism of JSF-2019 and its analogs may also lead to InhA and, more generally, FAS-II inhibition. The findings highlight a mechanism of action for nitro-containing antituberculars that should prove helpful in the effort to supplant delamanid and/or pretomanid.

STAR★METHODS

Detailed methods are provided in the online version of this paper and include the following:

- **KEY RESOURCES TABLE**
- **LEAD CONTACT AND MATERIALS AVAILABILITY**
- **EXPERIMENTAL MODEL AND SUBJECT DETAILS**
 - Mice
 - Bacterial Strains and Culture Conditions
- **METHOD DETAILS**
 - Minimum Inhibitory Concentration (MIC) Assay
 - Minimum Bactericidal Concentration (MBC) Assay
 - JSF-2019 Spontaneous Mutagenesis
 - RNA-Seq Analysis Method
 - Griess Assay for NO⁺ Quantification
 - Intrabacterial Drug Metabolism (IBDM) Assay
 - Physiochemical and ADME Profiling
 - Determination of Efficacy in an Intracellular Infection Model
 - 100-Day Culture Methods

- Mouse Pharmacokinetics (PK) Studies
- Mouse Acute Infection Model and Antibacterial Treatment
- Determination of InhA Percent Inhibition and IC₅₀
- Thin-Layer Chromatography (TLC) Analysis of Fatty Acids and Mycolic Acids
- Reduction of JSF-2019 to JSF-2026
- Synthetic Chemistry Methods
- Synthesis of Differentially Substituted Furans
- Syntheses of Differentially Linked Triazines
- Synthesis of Dialkylaminotriazines
- Synthesis of mono(amine)mono(morpholine)triazines
- **QUANTIFICATION AND STATISTICAL ANALYSIS**
- **DATA AND CODE AVAILABILITY**

SUPPLEMENTAL INFORMATION

Supplemental Information can be found online at <https://doi.org/10.1016/j.chembiol.2019.10.010>.

ACKNOWLEDGMENTS

J.S.F., N.C., and V.D. acknowledge support from award number U19AI109713 NIH/NIAID for the "Center to develop therapeutic countermeasures to high-threat bacterial agents," from the National Institutes of Health: Centers of Excellence for Translational Research (CETR). J.S.F. and S.E. acknowledge support from award number R41AI122434 "Optimization of small molecule triazine antituberculars for *in vivo* efficacy" from NIH/NIAID. Dr. John J. Piwinski is thanked for helpful discussions. We gratefully acknowledge access to the HPC facilities and support of the computational STEM and bioinformatics scientists from the Office of Advanced Research Computing (OARC) at Rutgers University. We further acknowledge the critical work made possible through access to the Perceval Linux cluster operated by OARC under NIH 1S10OD012346-01A1 and the Illumina NextSeq500 operated by the Genomics Center under NIH 1S10OD018206-01A1. Dr. John Eng, Mr. Saw Kyin, and Mr. Henry Shwe (Princeton University) are thanked for guidance with the HRMS studies. Biovia is kindly acknowledged for providing Discovery Studio.

AUTHOR CONTRIBUTIONS

X.W., D.I., R.R., S.-G.L., R.J., T.P.S., N.M., J.A.B., E.S., T.K., S.D.P., R.S.P., Y.-M.A., A.D.-P., S.K., C.G., S.H., M.D.Z., H.P.H., and S.P. performed the experiments. X.W., D.I., R.R., P.S., M.D.Z., V.D., S.E., N.C., P.K., and J.S.F. contributed to experimental design and data analysis. J.S.F., X.W., and D.I. wrote the manuscript, which was edited by all authors.

DECLARATION OF INTERESTS

The authors declare no competing interests.

Received: March 4, 2019

Revised: September 2, 2019

Accepted: October 22, 2019

Published: November 8, 2019

REFERENCES

- Albesa-Jove, D., Chiarelli, L.R., Makarov, V., Pasca, M.R., Urresti, S., Mori, G., Salina, E., Vocat, A., Comino, N., Mohorko, E., et al. (2014). Rv2466c mediates the activation of TP053 to kill replicating and non-replicating *Mycobacterium tuberculosis*. *ACS Chem. Biol.* 9, 1567–1575.
- Allison, B.D., Phuong, V.K., McAtee, L.C., Rosen, M., Morton, M., Prendergast, C., Barrett, T., Lagaud, G., Freedman, J., Li, L., et al. (2006). Identification and optimization of anthranilic sulfonamides as novel, selective cholecystokinin-2 receptor antagonists. *J. Med. Chem.* 49, 6371–6390.

- Andries, K., Verhasselt, P., Guillemont, J., Gohlmann, H.W., Neefs, J.M., Winkler, H., Van Gestel, J., Timmerman, P., Zhu, M., Lee, E., et al. (2005). A diarylquinoline drug active on the ATP synthase of *Mycobacterium tuberculosis*. *Science* 307, 223–227.
- Ashtekar, D.R., Costa-Perira, R., Nagrajan, K., Vishvanathan, N., Bhatt, A.D., and Rittel, W. (1993). In vitro and in vivo activities of the nitroimidazole CGI 17341 against *Mycobacterium tuberculosis*. *Antimicrob. Agents Chemother.* 37, 183–186.
- Awasthi, D., and Freundlich, J.S. (2017). Antimycobacterial metabolism: illuminating *Mycobacterium tuberculosis* biology and drug discovery. *Trends Microbiol.* 25, 756–767.
- Banerjee, A., Dubnau, E., Quemard, A., Balasubramanian, V., Um, K.S., Wilson, T., Collins, D., de Lisle, G., and Jacobs, W.R., Jr. (1994). inhA, a gene encoding a target for isoniazid and ethionamide in *Mycobacterium tuberculosis*. *Science* 263, 227–230.
- Blaser, A., Palmer, B.D., Sutherland, H.S., Kmentova, I., Franzblau, S.G., Wan, B., Wang, Y., Ma, Z., Thompson, A.M., and Denny, W.A. (2012). Structure-activity relationships for amide-, carbamate-, and urea-linked analogues of the tuberculosis drug (6S)-2-nitro-6-[[4-(trifluoromethoxy)benzyl]oxy]-6,7-dihydro-5H-imidazo[2,1-b][1,3]oxazine (PA-824). *J. Med. Chem.* 55, 312–326.
- Boshoff, H.I., Myers, T.G., Copp, B.R., McNeil, M.R., Wilson, M.A., and Barry, C.E., 3rd (2004). The transcriptional responses of *Mycobacterium tuberculosis* to inhibitors of metabolism: novel insights into drug mechanisms of action. *J. Biol. Chem.* 279, 40174–40184.
- Brickner, S.J., Hutchinson, D.K., Barbachyn, M.R., Manninen, P.R., Ulanowicz, D.A., Garmon, S.A., Grega, K.C., Hendges, S.K., Toops, D.S., Ford, C.W., et al. (1996). Synthesis and antibacterial activity of U-100592 and U-100766, two oxazolidinone antibacterial agents for the potential treatment of multidrug-resistant gram-positive bacterial infections. *J. Med. Chem.* 39, 673–679.
- Bruhin, H., Bühlmann, X., Hook, W.H., Hoyle, W., Orford, B., and Vischer, W. (1969). Antituberculosis activity of some nitrofur derivatives. *J. Pharm. Pharmacol.* 21, 423–433.
- Chakraborty, S., Gruber, T., Barry, C.E., 3rd, Boshoff, H.I., and Rhee, K.Y. (2013). Para-aminosalicylic acid acts as an alternative substrate of folate metabolism in *Mycobacterium tuberculosis*. *Science* 339, 88–91.
- Chaudhuri, S., Li, L., Zimmerman, M., Chen, Y., Chen, Y.X., Toosky, M.N., Gardner, M., Pan, M., Li, Y.Y., Kawaji, Q., et al. (2018). Kasugamycin potentiates rifampicin and limits emergence of resistance in *Mycobacterium tuberculosis* by specifically decreasing mycobacterial mistranslation. *Elife* 7, <https://doi.org/10.7554/eLife.36782>.
- Conradie, F., Diacon, A.H., Everitt, D., Mendel, C., van Niekerk, C., Howell, P., Comins, K., and Spigelman, M. (2017). The Nix-TB trial of pretomanid, bedaquiline and linezolid to treat XDR-TB. Paper presented at: Conference on Retroviruses and Opportunistic Infections (Seattle, Washington).
- Ding, A.H., Nathan, C.F., and Stuehr, D.J. (1988). Release of reactive nitrogen intermediates and reactive oxygen intermediates from mouse peritoneal macrophages. Comparison of activating cytokines and evidence for independent production. *J. Immunol.* 141, 2407–2412.
- Ekins, S., Reynolds, R.C., Kim, H., Koo, M.S., Ekonomidis, M., Talaue, M., Paget, S.D., Woolhiser, L.K., Lenaerts, A.J., Bunin, B.A., et al. (2013). Bayesian models leveraging bioactivity and cytotoxicity information for drug discovery. *Chem. Biol.* 20, 370–378.
- Feng, B.Y., and Shoichet, B.K. (2006). A detergent-based assay for the detection of promiscuous inhibitors. *Nat. Protoc.* 1, 550–553.
- Feng, B.Y., Simeonov, A., Jadhav, A., Babaoglu, K., Inglese, J., Shoichet, B.K., and Austin, C.P. (2007). A high-throughput screen for aggregation-based inhibition in a large compound library. *J. Med. Chem.* 50, 2385–2390.
- Franzblau, S.G., Witzig, R.S., McLaughlin, J.C., Torres, P., Madico, G., Hernandez, A., Degnan, M.T., Cook, M.B., Quenzer, V.K., Ferguson, R.M., et al. (1998). Rapid, low-technology MIC determination with clinical *Mycobacterium tuberculosis* isolates by using the microplate Alamar Blue assay. *J. Clin. Microbiol.* 36, 362–366.
- Freundlich, J.S., Wang, F., Vilcheze, C., Gulten, G., Langley, R., Schiehs, G.A., Jacobus, D.P., Jacobs, W.R., Jr., and Sacchettini, J.C. (2009). Triclosan derivatives: towards potent inhibitors of drug-sensitive and drug-resistant *Mycobacterium tuberculosis*. *ChemMedChem* 4, 241–248.
- Frohlich, T., and Tsogoeva, S.B. (2016). In vivo and in vitro optimization of screening antimalarial hits toward lead molecules for preclinical development. *J. Med. Chem.* 59, 9668–9671.
- Geiter, L. (2017). Delamanid global clinical database and phase 3 trial results. Paper presented at: Satellite symposium presentation at the 48th Union World Conference on Lung Health (Guadalajara, Mexico).
- Gupta, A. (2017). SNPTB: nucleotide variant identification and annotation in *Mycobacterium tuberculosis* genomes. *BioRxiv*. <https://doi.org/10.1101/227066>.
- Gurumurthy, M., Mukherjee, T., Dowd, C.S., Singh, R., Niyomrattanakit, P., Tay, J.A., Nayyar, A., Lee, Y.S., Cherian, J., Boshoff, H.I., et al. (2012). Substrate specificity of the deazaflavin-dependent nitroreductase from *Mycobacterium tuberculosis* responsible for the bioreductive activation of bicyclic nitroimidazoles. *FEBS J.* 279, 113–125.
- Gurumurthy, M., Rao, M., Mukherjee, T., Rao, S.P., Boshoff, H.I., Dick, T., Barry, C.E., 3rd, and Manjunatha, U.H. (2013). A novel F(420)-dependent anti-oxidant mechanism protects *Mycobacterium tuberculosis* against oxidative stress and bactericidal agents. *Mol. Microbiol.* 87, 744–755.
- Harper, J., Skerry, C., Davis, S.L., Tasneen, R., Weir, M., Kramnik, I., Bishai, W.R., Pomper, M.G., Nuernberger, E.L., and Jain, S.K. (2012). Mouse model of necrotic tuberculosis granulomas develops hypoxic lesions. *J. Infect. Dis.* 205, 595–602.
- Haver, H.L., Chua, A., Ghode, P., Lakshminarayana, S.B., Singhal, A., Mathema, B., Wintjens, R., and Bifani, P. (2015). Mutations in genes for the F420 biosynthetic pathway and a nitroreductase enzyme are the primary resistance determinants in spontaneous in vitro-selected PA-824-resistant mutants of *Mycobacterium tuberculosis*. *Antimicrob. Agents Chemother.* 59, 5316–5323.
- Hoffmann, H., Kohl, T.A., Hofmann-Thiel, S., Merker, M., Beckert, P., Jatón, K., Nedialkova, L., Sahalchik, E., Rothe, T., Keller, P.M., et al. (2016). Delamanid and bedaquiline resistance in *Mycobacterium tuberculosis* ancestral Beijing genotype causing extensively drug-resistant tuberculosis in a Tibetan refugee. *Am. J. Resp. Crit. Care Med.* 193, 337–340.
- Hu, Y., and Coates, A.R. (2011). *Mycobacterium tuberculosis* acg gene is required for growth and virulence in vivo. *PLoS One* 6, e20958.
- Hu, Y., Coates, A.R., and Mitchison, D.A. (2003). Sterilizing activities of fluoroquinolones against rifampin-tolerant populations of *Mycobacterium tuberculosis*. *Antimicrob. Agents Chemother.* 47, 653–657.
- Inoyama, D., Paget, S.D., Russo, R., Kandasamy, S., Kumar, P., Singleton, E., Occi, J., Tuckman, M., Zimmerman, M.D., Ho, H.P., et al. (2018). Novel pyrimidines as antitubercular agents. *Antimicrob. Agents Chemother.* 62, <https://doi.org/10.1128/AAC.02063-17>.
- Kumar, P., Capodagli, G.C., Awasthi, D., Shrestha, R., Maharaja, K., Sukheja, P., Li, S.G., Inoyama, D., Zimmerman, M., Ho Liang, H.P., et al. (2018). Synergistic lethality of a binary inhibitor of *Mycobacterium tuberculosis* KasA. *MBio* 9, <https://doi.org/10.1128/mBio.02101-17>.
- Lanoix, J.P., Tasneen, R., O'Brien, P., Sarathy, J., Safi, H., Pinn, M., Alland, D., Dartois, V., and Nuernberger, E. (2016). High systemic exposure of pyrazinoid acid has limited antituberculosis activity in murine and rabbit models of tuberculosis. *Antimicrob. Agents Chemother.* 60, 4197–4205.
- Li, S.Y., Tasneen, R., Tyagi, S., Soni, H., Converse, P.J., Mdluli, K., and Nuernberger, E.L. (2017). Bactericidal and sterilizing activity of a novel regimen with bedaquiline, pretomanid, moxifloxacin, and pyrazinamide in a murine model of tuberculosis. *Antimicrob. Agents Chemother.* 61, <https://doi.org/10.1128/AAC.00913-17>.
- MacMicking, J.D., North, R.J., LaCourse, R., Mudgett, J.S., Shah, S.K., and Nathan, C.F. (1997). Identification of nitric oxide synthase as a protective locus against tuberculosis. *Proc. Natl. Acad. Sci. U S A* 94, 5243–5248.

- Manjunatha, U., Boshoff, H.I., and Barry, C.E. (2009). The mechanism of action of PA-824: novel insights from transcriptional profiling. *Commun. Integr. Biol.* 2, 215–218.
- Manjunatha, U.H., Boshoff, H., Dowd, C.S., Zhang, L., Albert, T.J., Norton, J.E., Daniels, L., Dick, T., Pang, S.S., and Barry, C.E., 3rd (2006). Identification of a nitroimidazo-oxazine-specific protein involved in PA-824 resistance in *Mycobacterium tuberculosis*. *Proc. Natl. Acad. Sci. U S A* 103, 431–436.
- Matsumoto, M., Hashizume, H., Tomishige, T., Kawasaki, M., Tsubouchi, H., Sasaki, H., Shimokawa, Y., and Komatsu, M. (2006). OPC-67683, a nitro-dihydro-imidazooxazole derivative with promising action against tuberculosis in vitro and in mice. *PLoS Med.* 3, e466.
- Mehta, P.K., King, C.H., White, E.H., Murtagh, J.J., and Quinn, F.D. (1996). Comparison of in vitro models for the study of *Mycobacterium tuberculosis* invasion and intracellular replication. *Infect. Immun.* 64, 2673–2679.
- Murray, S. (2016). NC-005: Phase 2 clinical trial results of bedaquiline, moxifloxacin, pretomanid, and pyrazinamide for drug-sensitive and drug-resistant TB. Paper presented at: Satellite symposium presentation at the 47th Union World Conference on Lung Health (Liverpool, England).
- Negri, A., Javidnia, P., Mu, R., Zhang, X., Vendome, J., Gold, B., Roberts, J., Barman, D., Ioerger, T., Sacchetti, J.C., et al. (2018). Identification of a mycothiol-dependent nitroreductase from *Mycobacterium tuberculosis*. *ACS Infect. Dis.* 4, 771–787.
- Palmer, B.D., Sutherland, H.S., Blaser, A., Kmentova, I., Franzblau, S.G., Wan, B., Wang, Y., Ma, Z., Denny, W.A., and Thompson, A.M. (2015). Synthesis and structure-activity relationships for extended side chain analogues of the anti-tubercular drug (6S)-2-nitro-6-[[4-(trifluoromethoxy)benzyl]oxy]-6,7-dihydro-5H-imidazo[2,1-b][1,3]oxazine (PA-824). *J. Med. Chem.* 58, 3036–3059.
- Parikh, S., Moynihan, D.P., Xiao, G., and Tonge, P.J. (1999). Roles of tyrosine 158 and lysine 165 in the catalytic mechanism of InhA, the enoyl-ACP reductase from *Mycobacterium tuberculosis*. *Biochemistry* 38, 13623–13634.
- Purkayastha, A., McCue, L.A., and McDonough, K.A. (2002). Identification of a *Mycobacterium tuberculosis* putative classical nitroreductase gene whose expression is coregulated with that of the *acr* gene within macrophages, in standing versus shaking cultures, and under low oxygen conditions. *Infect. Immun.* 70, 1518–1529.
- Rao, S.P.S., Lakshminarayana, S.B., Kondreddi, R.R., Herve, M., Camacho, L.R., Bifani, P., Kalapala, S.K., Jiricek, J., Ma, N.L., Tan, B.H., et al. (2013). Indolcarboxamide is a preclinical candidate for treating multidrug-resistant tuberculosis. *Sci. Transl. Med.* 5, 214ra168.
- Rawat, R., Whitty, A., and Tonge, P.J. (2003). The isoniazid-NAD adduct is a slow, tight-binding inhibitor of InhA, the *Mycobacterium tuberculosis* enoyl reductase: adduct affinity and drug resistance. *Proc. Natl. Acad. Sci. U S A* 100, 13881–13886.
- Rengarajan, J., Bloom, B.R., and Rubin, E.J. (2005). Genome-wide requirements for *Mycobacterium tuberculosis* adaptation and survival in macrophages. *Proc. Natl. Acad. Sci. U S A* 102, 8327–8332.
- Rifat, D., Li, S.-Y., Ioerger, T., Lanoix, J.-P., Lee, J., Bashiri, G., Sacchetti, J., and Nuermberger, E. (2018). Mutations in Rv2983 as a novel determinant of resistance to nitroimidazole drugs in *Mycobacterium tuberculosis*. *bioRxiv*. <https://doi.org/10.1101/457754>.
- Robinson, M.D., McCarthy, D.J., and Smyth, G.K. (2010). edgeR: a Bioconductor package for differential expression analysis of digital gene expression data. *Bioinformatics* 26, 139–140.
- Rosado, L.A., Wahn, K., Degiacomi, G., Pedre, B., Young, D., de la Rubia, A.G., Boldrin, F., Martens, E., Marcos-Pascual, L., Sancho-Vaello, E., et al. (2017). The antibacterial prodrug activator Rv2466c is a mycothiol-dependent reductase in the oxidative stress response of *Mycobacterium tuberculosis*. *J. Biol. Chem.* 292, 13097–13110.
- Rozwarski, D.A., Grant, G.A., Barton, D.H.R., Jacobs, W.R., Jr., and Sacchetti, J.C. (1998). Modification of the NADH of the isoniazid target (InhA) from *Mycobacterium tuberculosis*. *Science* 279, 98–102.
- Sarathy, J., Dartois, V., Dick, T., and Gengenbacher, M. (2013). Reduced drug uptake in phenotypically resistant nutrient-starved nonreplicating *Mycobacterium tuberculosis*. *Antimicrob. Agents Chemother.* 57, 1648–1653.
- Scott, J.S., Gill, A.L., Godfrey, L., Groombridge, S.D., Rees, A., Revill, J., Schofield, P., Sorme, P., Stocker, A., Swales, J.G., et al. (2012). Optimisation of pharmacokinetic properties in a neutral series of 11beta-HSD1 inhibitors. *Bioorg. Med. Chem. Lett.* 22, 6756–6761.
- Shoichet, B.K. (2006). Interpreting steep dose-response curves in early inhibitor discovery. *J. Med. Chem.* 49, 7274–7277.
- Singh, R., Manjunatha, U., Boshoff, H.I., Ha, Y.H., Niyomrattanakit, P., Ledwidge, R., Dowd, C.S., Lee, I.Y., Kim, P., Zhang, L., et al. (2008). PA-824 kills nonreplicating *Mycobacterium tuberculosis* by intracellular NO release. *Science* 322, 1392–1395.
- Sivaraman, S., Zwahlen, J., Bell, A.F., Hedstrom, L., and Tonge, P.J. (2003). Structure-activity studies of the inhibition of FabI, the enoyl reductase from *Escherichia coli*, by triclosan: kinetic analysis of mutant FabIs. *Biochemistry* 42, 4406–4413.
- Slayden, R.A., and Barry, C.E., 3rd (2001). Analysis of the lipids of *Mycobacterium tuberculosis*. *Methods Mol. Med.* 54, 229–245.
- Stec, J., Vilcheze, C., Lun, S., Perryman, A.L., Wang, X., Freundlich, J.S., Bishai, W., Jacobs, W.R., Jr., and Kozikowski, A.P. (2014). Biological evaluation of potent triclosan-derived inhibitors of the enoyl-acyl carrier protein reductase InhA in drug-sensitive and drug-resistant strains of *Mycobacterium tuberculosis*. *ChemMedChem* 9, 2528–2537.
- Stover, C.K., Warren, P., VanDevanter, D.R., Sherman, D.R., Arain, T.M., Langhorne, M.H., Anderson, S.W., Towell, J.A., Yuan, Y., McMurray, D.N., et al. (2000). A small-molecule nitroimidazopyran drug candidate for the treatment of tuberculosis. *Nature* 405, 962–966.
- Summa, V., Petrocchi, A., Matassa, V.G., Gardelli, C., Muraglia, E., Rowley, M., Paz, O.G., Laufer, R., Monteagudo, E., and Pace, P. (2006). 4,5-Dihydroxypyrimidine carboxamides and N-alkyl-5-hydroxypyrimidinone carboxamides are potent, selective HIV integrase inhibitors with good pharmacokinetic profiles in preclinical species. *J. Med. Chem.* 49, 6646–6649.
- Tan, M.P., Sequeira, P., Lin, W.W., Phong, W.Y., Cliff, P., Ng, S.H., Lee, B.H., Camacho, L., Schnappinger, D., Ehr, S., et al. (2010). Nitrate respiration protects hypoxic *Mycobacterium tuberculosis* against acid- and reactive nitrogen species stresses. *PLoS One* 5, e13356.
- Thompson, A.M., Bonnet, M., Lee, H.H., Franzblau, S.G., Wan, B., Wong, G.S., Cooper, C.B., and Denny, W.A. (2017). Antitubercular nitroimidazoles revisited: synthesis and activity of the authentic 3-nitro isomer of pretomanid. *ACS Med. Chem. Lett.* 8, 1275–1280.
- Thompson, A.M., Sutherland, H.S., Palmer, B.D., Kmentova, I., Blaser, A., Franzblau, S.G., Wan, B., Wang, Y., Ma, Z., and Denny, W.A. (2011). Synthesis and structure-activity relationships of varied ether linker analogues of the antitubercular drug (6S)-2-nitro-6-[[4-(trifluoromethoxy)benzyl]oxy]-6,7-dihydro-5H-imidazo[2,1-b][1,3]oxazine (PA-824). *J. Med. Chem.* 54, 6563–6585.
- Twarog, N.R., Stewart, E., Hammill, C.V., and Shelat, A.A. (2016). BRAID: a unifying paradigm for the analysis of combined drug action. *Sci. Rep.* 6, 25523.
- van Soolingen, D., Hermans, P.W., de Haas, P.E., Soll, D.R., and van Embden, J.D. (1991). Occurrence and stability of insertion sequences in *Mycobacterium tuberculosis* complex strains: evaluation of an insertion sequence-dependent DNA polymorphism as a tool in the epidemiology of tuberculosis. *J. Clin. Microbiol.* 29, 2578–2586.
- Vilcheze, C., Baughn, A.D., Tufariello, J., Leung, L.W., Kuo, M., Basler, C.F., Alland, D., Sacchetti, J.C., Freundlich, J.S., and Jacobs, W.R., Jr. (2011). Novel inhibitors of InhA efficiently kill *Mycobacterium tuberculosis* under aerobic and anaerobic conditions. *Antimicrob. Agents Chemother.* 55, 3889–3898.
- Vilcheze, C., Wang, F., Arai, M., Hazbon, M.H., Colangeli, R., Kremer, L., Weisbrod, T.R., Alland, D., Sacchetti, J.C., and Jacobs, W.R., Jr. (2006). Transfer of a point mutation in *Mycobacterium tuberculosis* inhA resolves the target of isoniazid. *Nat. Med.* 12, 1027–1029.

- Voskuil, M.I., Bartek, I.L., Visconti, K., and Schoolnik, G.K. (2011). The response of mycobacterium tuberculosis to reactive oxygen and nitrogen species. *Front. Microbiol.* 2, 105.
- WHO (2018). Global Tuberculosis Report 2018 (World Health Organization).
- Wilson, M., DeRisi, J., Kristensen, H.H., Imboden, P., Rane, S., Brown, P.O., and Schoolnik, G.K. (1999). Exploring drug-induced alterations in gene expression in *Mycobacterium tuberculosis* by microarray hybridization. *Proc. Natl. Acad. Sci. U S A* 96, 12833–12838.
- Wilson, R., Kumar, P., Parashar, V., Vilcheze, C., Veyron-Churlet, R., Freundlich, J.S., Barnes, S.W., Walker, J.R., Szymonifka, M.J., Marchiano, E., et al. (2013). Antituberculosis thiophenes define a requirement for Pks13 in mycolic acid biosynthesis. *Nat. Chem. Biol.* 9, 499–506.
- Zhang, Y., Heym, B., Allen, B., Young, D., and Cole, S. (1992). The catalase-peroxidase gene and isoniazid resistance of *Mycobacterium tuberculosis*. *Nature* 358, 591–593.

STAR★METHODS

KEY RESOURCES TABLE

REAGENT or RESOURCE	SOURCE	IDENTIFIER
Bacterial and Virus Strains		
<i>M. tuberculosis</i> strain H37Rv	Lab stock	BEI NR-13648
<i>M. tuberculosis</i> strain CDC1551	Lab stock	BEI NR-13649
<i>M. tuberculosis</i> transposon library with H37Rv background (H37Rv::tn)	Professor Christopher Sassetti's Lab	N/A
<i>M. tuberculosis</i> Δ leu Δ panCD auxotroph strain mc ² 6206	Professor William R. Jacobs' Lab	N/A
<i>M. tuberculosis</i> katG mutant (KatG S315T)	Professor David Alland's Lab	DRM12
<i>M. tuberculosis</i> clinical strain TDR31 resistant to INH, RIF, EMB, KAN, SM, CAP	Special Programme for Research and Training in Tropical Diseases (TDR) established by UNICEF/UNDP/World Bank/WHO Special Programs (Through Pradeep Kumar in Professor David Alland's lab)	TDR31
<i>M. tuberculosis</i> clinical strain TDR36 resistant to INH, RIF, EMB	Special Programme for Research and Training in Tropical Diseases (TDR) established by UNICEF/UNDP/World Bank/WHO Special Programs (Through Pradeep Kumar in Professor David Alland's lab)	TDR36
<i>M. tuberculosis</i> clinical strain TDR116 resistant to INH, EMB, PAS	Special Programme for Research and Training in Tropical Diseases (TDR) established by UNICEF/UNDP/World Bank/WHO Special Programs (Through Pradeep Kumar in Professor David Alland's lab)	TDR116
<i>E. coli</i> chemically competent TOP10	ThermoFisher	Cat# C40005
<i>E. coli</i> chemically competent BL21(DE3)pLysE	ThermoFisher	C656503
Chemicals, Peptides, and Recombinant Proteins		
Small molecules labeled as JSF-#	This paper; Freundlich Lab	
Pretomanid	AdooQ Bioscience	Cat# A11401-50
Isoniazid (INH)	Sigma-Aldrich	Cat# 75182-50MG
Rifampicin (RIF)	Carbosynth	Cat# AR11351
β -Nicotinamide adenine dinucleotide, reduced dipotassium salt (β -NADH)	Sigma-Aldrich	Cat# N4505-500MG
trans-2-dodecenoyl-CoA (DD-CoA)	Freundlich Lab	N/A
Resazurin sodium salt	Sigma-Aldrich	Cat# R7017-5G
TRIZOL™ Reagent	ThermoFisher	Cat# 15596018
<i>M. tuberculosis</i> protein InhA expressed in <i>E. coli</i>	This paper; Freundlich Lab	N/A
Critical Commercial Assays		
Griess Reagent Kit. for nitrite quantitation	ThermoFisher	Cat# G7921
Vybrant MTT Cell Proliferation Assay Kit	ThermoFisher	Cat# V13154
AlamarBlue™ Dye	ThermoFisher	Cat# Y00-025
RNeasy Mini Kit	Qiagen	Cat# 74106
Nextera XT DNA Library Kit	Illumina	Cat# FC-131-1096
Nextera XT Index Kit (24 indexes, 96 samples)	Illumina	Cat# FC-131-1001
Ribo Zero kit	Illumina	Cat# MRZB12424
NEBNext Ultra II RNA library prep kit	New England Biolabs	Cat# 7770

(Continued on next page)

Continued

REAGENT or RESOURCE	SOURCE	IDENTIFIER
Deposited Data		
Raw and analyzed RNA-seq data	This paper	NCBI Gene Expression Omnibus (GEO), GSE126718
Transcriptional responses of <i>M. tuberculosis</i> to inhibitors of metabolism	NCBI Gene Expression Omnibus (Boshoff et al., 2004)	GEO: GSE1642
Transcriptional response of <i>M. tuberculosis</i> to reactive oxygen and nitrogen species	NCBI Gene Expression Omnibus (Voskuil et al., 2011)	GEO: GSE16146
Whole-genome sequencing data of <i>M. tuberculosis</i> mutants against JSF-2019	This paper	NCBI Sequence Read Archive (SRA), access code PRJNA521574
Experimental Models: Cell Lines		
J774.1 mouse macrophage	ATCC	ATCC TIB-67
Vero cell (African green monkey kidney)	ATCC	ATCC CCL-81
Experimental Models: Organisms/Strains		
Mouse: 6-week-old-female outbred CD-1 IGS	Charles River Labs	CrI:CD1(ICR), strain code 022
Mouse: 9-week-old female BALB/c	Charles River Labs	BALB/cAnNCrI, strain code 028
Oligonucleotides		
Primer for <i>fgd1</i> amplification from <i>M. tuberculosis</i> Forward: GAGGCATTCTCCCGGTATTC	This paper	N/A
Primer for <i>fgd1</i> amplification from <i>M. tuberculosis</i> Reverse: GCAGAGAGCCGCGTAATC	This paper	N/A
Primer for cloning <i>M. tuberculosis inhA</i> Forward: GACGCATATGACAGGACTGCTGGAC	This paper	N/A
Primer for cloning <i>M. tuberculosis inhA</i> Reverse: GGCGGATCCTAGAGCAATTGGGTG	This paper	N/A
Recombinant DNA		
Vector pET15b	Millipore sigma	Cat# 69661
Software and Algorithms		
GraphPad Prism	GraphPad software Inc	https://www.graphpad.com/scientific-software/prism/
SnapGene	GSL Biotech LLC	https://www.snapgene.com/
R package 'pheatmap'	Raivo Kolde	https://CRAN.R-project.org/package=pheatmap
R package 'braidrm'	Twarog et al., 2016	https://CRAN.R-project.org/package=braidrm
R package 'braidReports'	Twarog et al., 2016	https://CRAN.R-project.org/package=braidReports
SNPTB for mapping Illumina whole-genome sequencing data to reference	Gupta, 2017	https://github.com/aditi9783/SNPTB

LEAD CONTACT AND MATERIALS AVAILABILITY

Further information and requests for reagents may be forwarded to the corresponding author Joel S. Freundlich (freundjs@rutgers.edu). All unique/stable reagents generated in this study are available from the Lead Contact without restriction.

EXPERIMENTAL MODEL AND SUBJECT DETAILS**Mice**

Animal studies were carried out in accordance with the guide for the care and use of Laboratory Animals of the National Institutes of Health, with approval from the Institutional Animal Care and Use Committee (IACUC) of the New Jersey Medical School, Rutgers University, Newark. All animals were maintained under specific pathogen-free conditions and fed water and chow *ad libitum*, and all efforts were made to minimize suffering or discomfort. Mouse PK studies used 6-week-old female outbred CD-1 mice (Charles River Labs, Wilmington, MA). 9-week-old female BALB/c mice (19-20 g, Charles River Labs, Wilmington, MA) were used for the mouse acute infection model.

Bacterial Strains and Culture Conditions

M. tuberculosis strains H37Rv (BEI NR-13648) and CDC1551 (BEI NR-13649) are from our laboratory's stock. *M. tuberculosis* transposon library with H37Rv background (H37Rv::tn) was a kind gift from Professor Christopher Sassetti's laboratory. *M. tuberculosis* Δ leu Δ panCD auxotroph strain mc²6206 and *inhA* promoter mutation (c(-15)t) strain mc²4914 were kind gifts from the laboratory of Professor William R. Jacobs, Jr. *M. tuberculosis* strains were grown at 37°C in Difco Middlebrook 7H9 (BD) medium with 0.2% (v/v) glycerol, 10% (v/v) ADS (0.5% bovine serum albumin (BSA, Fisher), 0.2% dextrose, 0.085% NaCl), and 0.05% tyloxapol (7H9+ADS+tyloxapol). Transposon strains with the kanamycin resistance marker were cultured with 7H9+ADS+tyloxapol media supplemented with kanamycin at 20 µg/mL.

METHOD DETAILS

Minimum Inhibitory Concentration (MIC) Assay

MIC values of the compounds were determined following the microplate-based Alamar Blue assay (MABA) method as previously described (Franzblau et al., 1998). Twofold series dilutions of compounds were prepared in sterile polystyrene 96-well round-bottom plate (CLS3795, Corning, NY) with Middlebrook 7H9+ADS media (no tyloxapol) as 100 µL per well. *M. tuberculosis* strains were 1:1000 diluted in 7H9+ADS medium at mid-logarithmic stage of growth (OD₅₉₅ = 0.4). 50 µL of diluted bacteria suspensions were inoculated into each well, followed by incubation at 37°C for 7 d. 20 µL alamarBlue® reagent (Invitrogen, Frederick, MD), freshly mixed with 12.5 µL 20% Tween 80, was added into each well, followed by 24-h incubation at 37°C. Absorbance was read at 570 nm, with reference wavelength 600 nm, using a microplate reader (ELX808, Biotek Instruments). The MIC endpoint was defined as the lowest concentration of the test agent that produced at least 90% reduction in absorbance compared with that of the drug-free control.

Minimum Bactericidal Concentration (MBC) Assay

To determine the minimum bactericidal concentration (MBC) against *M. tuberculosis*, the bacterial cultures from the 96-well plates utilized for the compound MIC determination instead of undergoing Alamar Blue addition were re-suspended, serially diluted with sterile PBS and plated on Middlebrook 7H11 plates. Colony-forming units (CFUs) were enumerated following 21-d incubation at 37°C. The MBC was reported as the minimum compound concentration at which a 2 log₁₀ reduction in CFUs was observed as compared to the no-compound control.

JSF-2019 Spontaneous Mutagenesis

Compound JSF-2019 was supplemented into 7H10 agar plates with 10% (v/v) ADS and 0.5% glycerol at 5x, 10x, 20x, and 30x MIC. Mid-log phase of *M. tuberculosis* H37Rv culture (OD₅₉₅ = 0.4) was harvested and concentrated to ~10⁹ CFU/mL in fresh medium 7H9+ADS followed by CFU enumeration. 100 µL of culture (~10⁸ CFU) was streaked on JSF-2019 containing agar plates followed by incubation at 37°C for 4 to 6 weeks. Single colonies were isolated followed by liquid MIC test for resistance verification. For resistant colonies of interest, genomic DNA was isolated (van Soolingen et al., 1991). Genomic libraries were prepared using the Nextera XP Library Prep Kit (Illumina, San Diego, CA) prior to sequencing on the Illumina NextSeq Platform (Illumina, San Diego, CA). Sequence reads were aligned to reference strain H37Rv (AL123456.3) and analyzed for single nucleotide polymorphisms (SNPs) using the SNPTB platform (Gupta, 2017).

RNA-Seq Analysis Method

Total RNA was extracted by using Trizol (Invitrogen) followed by Qiagen RNeasy kit purification using the standard protocol. The quality of RNA was checked on an Agilent 2100 Bioanalyzer using the RNA pico6000 kit; samples with RNA integrity number >7.0 were used for subsequent processing. Illumina Ribo-Zero rRNA Removal Kit (Bacteria) was used for the removal of ribosomal RNA according to the manufacturer's protocol. The Illumina compatible RNA-seq library was prepared using the NEBNext ultra RNAseq library preparation kit. The cDNA libraries were purified using AmpureXP beads and quantified on an Agilent 2100 Bioanalyzer as well as a Qubit 2.0 Fluorometer (Life Technologies, Carlsbad, CA). An equimolar amount of barcoded libraries were pooled and sequenced on an Illumina NextSeq 500 (Illumina, San Diego, CA) with 1x75 configuration. CLC Genomics Workbench 10.0.1 version (CLC, Bio-QIAGEN, Aarhus, Denmark) was used for RNA-Seq analysis. De-multiplexed FASTQ files from RNA-Seq libraries were imported into the CLC software. Bases with low quality were trimmed and reads were mapped to the reference genome, *M. tuberculosis* H37Rv (GenBank ID: NC_000962.3). The aligned reads were obtained and differential expression for RNA-seq data was carried out using multi-factorial statistics based on a negative binomial Generalized Linear Model (GLM) (Robinson et al., 2010), an RNA-seq tool in the CLC Genomic Workbench. Replicates were averaged and differentially expressed significant genes with FDR p-value <0.05 and fold change of an absolute value >1.5 for the three comparisons were calculated.

Griess Assay for NO⁺ Quantification

Griess reagent (Invitrogen, G7921) was applied to quantify NO⁺ release from the *M. tuberculosis* strain in the presence of compound. *M. tuberculosis* strains were grown to mid-log phase (OD₅₉₅ = 0.3) followed by compound treatment. At each time point, the supernatant of the culture aliquot was added to a 96-well plate in triplicate (200 µL/well). 20 µL of Griess reagent mix was added into each

well followed by incubation at room temperature for 30 min. Results were read at an absorbance of 548 nm, and sample nitrite concentration was converted from absorbance reading according to a nitrite calibration curve.

Intrabacterial Drug Metabolism (IBDM) Assay

An *M. tuberculosis* culture was grown to mid-log phase ($OD_{595} = 0.6$; $\sim 2 \times 10^8$ CFU/mL) in 7H9+ADS+tyloxapol for each compound treatment at a desired concentration. After 24 h, the cell pellet was harvested by centrifugation (10,000 rpm for 10 min at 4°C). The washed pellet was quenched with CH₃CN/CH₃OH/water (2:2:1) pre-chilled on dry ice, followed by lysis via bead beating (6.5 m/s, 30 s, 6 times). In between each round of bead beating, the sample was chilled on ice for 2 min to avoid overheating. The pellet metabolite extract in organic solvent was collected via 0.22 μ m filtration. After a proper decontamination process, both culture supernatant and pellet extract were brought out of the BSL-3 for further analysis.

We typically applied an Agilent 1260 HPLC coupled with an Agilent 6120 quadrupole mass spectrum for metabolomics analysis. Metabolites were separated on a Chromolith SpeedRod column with a gradient of H₂O and acetonitrile acidified with 0.1% formic acid. The mass resolution ranged from 10 to 2000 Da with an accuracy of ± 0.13 Da within the calibrated mass range in scan mode. After extraction and purification of a certain metabolite from cell lysate, its structure was confirmed by comparison of its ¹H NMR spectrum (Bruker Avance 500 MHz spectrometer), LC-MS spectrum (Agilent 6120 single quadrupole LC/MS system) and high-resolution mass (Agilent 6220 accurate-mass time-of-flight or Thermo LTQ Orbitrap XL) with those for an authentic/independently synthesized sample. Signal intensity was quantified by standard curve for an authentic/independently synthesized sample, and normalized by sample protein concentration determined via the Pierce BCA protein assay kit.

Physiochemical and ADME Profiling

This set of assays was performed by BioDuro, Incorporated. Mouse and human liver microsomal stability were determined via the following protocol. Working solutions of test compound were prepared in DMSO and diluted to a final concentration of 100 μ M in 50 mM phosphate buffer (pH 7.4). Aliquots of mouse or human liver microsome working solution were transferred into Eppendorf tubes using a multichannel pipette. Positive control (midazolam) and test compound working solutions were transferred into the tubes. The mixtures were vortexed gently and then pre-incubated at 37°C. Buffer with or without 5 mM NADPH was aliquoted into the tubes using a multichannel pipette and vortexed gently. At each time point of 0, 5, 15, 30, and 60 min with NADPH or 0, 30, and 60 min without NADPH, terfenadine/tolbutamide in acetonitrile/MeOH (1:1 v/v) was added to the reaction mixture to quench and precipitate the microsomal incubations. Samples were capped and vigorously vortexed and then centrifuged at 4°C. An aliquot of each supernatant was transferred for LC-MS/MS analysis. The MS detection was performed by using a SCIEX API 4000 QTRAP instrument. Each compound was analyzed by reverse-phase HPLC using a Kinetex 2.6 μ C18 100Å column (3.0 mm X 30 mm, Phenomenex) with the mobile phase consisting of solvent A: water with 0.1% formic acid, solvent B: acetonitrile with 0.1% formic acid. The amount of parent compound was determined on the basis of the peak area ratio (compound area to internal standard area) at each time point, enabling the determination of the compound half-life, $t_{1/2}$. The estimation of Cl_{int} (in μ L/min/mg protein) was calculated using Equation 1:

$$Cl_{int} = \frac{\ln(2) \times 1000 \times [protein]}{t_{1/2}} \quad (\text{Equation 1})$$

Kinetic aqueous solubility was quantified by the following approach. Dilutions of test compound solution were prepared in DMSO. 4 μ L of each dilution of the test compound in DMSO was added to 396 μ L of the universal aqueous buffer (pH = 7.4; 45 mM ethanolamine, 45 mM KH₂PO₄, 45 mM potassium acetate, 75 mM KCl) to afford a final DMSO concentration ranging between 0.002 μ M and 200 μ M. Three replicates of each test compound were prepared per concentration. After 4 h shaking at rt, the mixture was further incubated without shaking for 30 min at rt and then was filtered. The filtrate was diluted 10x and 30x with DMSO before LC-MS/MS analysis. Standard solutions were prepared as follows: stock solutions were diluted to ten defined concentration points from 60 μ M to 0.002 μ M with DMSO. Aliquots of samples and standard solutions were filtered and mixed with acetonitrile/H₂O, then vortexed and used for LC-MS/MS analysis. The MS detection was performed by using a SCIEX API 4000 QTRAP instrument. Each compound was analyzed by reverse-phase HPLC using a Kinetex 2.6 μ C18 100 Å column (3.0 mm X 30 mm, Phenomenex) with the mobile phase consisting of solvent A: water with 0.1% formic acid, solvent B: acetonitrile with 0.1% formic acid. The amount of parent compound was determined on the basis of the peak area ratio (compound area to internal standard area) for each time point. The solubility of the test compound was determined based on the largest calculated concentration amongst the samples.

Mouse and human plasma protein binding and stability were measured with the following procedure. Working solutions (1 mM in DMSO) were prepared for each test and control compound. The dosing solutions were prepared by diluting the working solutions to 5 μ M in plasma. The dialysis plate was prepared by adding buffer to one chamber and dosing solution to the other chamber. The plate was sealed with an adhesive film and incubated at 37°C while shaking for 5 h. Equal volumes of post dialysis samples were removed from both the plasma and the buffer chambers and placed in separate microcentrifuge tubes and equal volumes (50 μ L) of fresh phosphate buffer and plasma were added to the tubes, respectively. Plasma samples were diluted 5-fold and then all samples were treated with quenching solution (terfenadine/tolbutamide in 1:1 v/v methanol/acetonitrile). Sample mixtures were then centrifuged, and the supernatant was subjected to LC-MS/MS analysis. To assess plasma stability, aliquots of dosing solution were stored at 4°C ($t = 0$ h sample) and at 37°C for 5 h ($t = 5$ h sample). Following incubation, aliquots were subjected to LC-MS/MS analysis. The MS detection was performed by using a SCIEX API 4000 QTRAP instrument. Each compound was analyzed by reverse-phase HPLC

using a Kinetex 2.6 μ C18 100 Å column (3.0 mm X 30 mm, Phenomenex) with the mobile phase consisting of solvent A: water with 0.1% formic acid, solvent B: acetonitrile with 0.1% formic acid. The amount of parent compound was determined on the basis of the peak area ratio (compound area to internal standard area) for each time point. The percent plasma protein binding was calculated according to Equation 2, where Cpe is the concentration of test compound in plasma at equilibrium and Cb is the concentration of test compound in buffer at equilibrium, and the percent plasma stability was determined via Equation 3:

$$\% \text{ Binding} = \frac{C_{pe} - C_b}{C_{pe}} \times 100 \quad (\text{Equation 2})$$

$$\% \text{ Stability of test compound} = \frac{[\text{stability sample}]}{[\text{time zero sample}]} \times 100 \quad (\text{Equation 3})$$

Human cytochrome P450 inhibition was assayed via the following methodology. Pooled human liver microsomes were used as the enzyme source, and phenacetin (CYP1A2, 10 μ M), diclofenac (CYP2C9, 10 μ M), omeprazole (CYP2C19, 0.5 μ M), dextromethorphan (CYP2D6, 5 μ M), and midazolam (CYP3A4, 5 μ M) as probe substrates. The assay mixture (200 μ L total volume) contained test compound (each with final concentrations in the 0 – 50 μ M range) and human liver microsomes (final concentration of 0.25 mg protein per mL) with or without NADPH (final concentration of 1.0 mM) in 100 mM phosphate buffer (pH 7.4). After a 20 min incubation at 37°C, the mixture was quenched by adding 300 μ L of methanol/acetonitrile (1:1 v/v) containing terfenadine and tolbutamide. The sample was then centrifuged at 4,000 rpm for 15 min at 4°C. 100 μ L supernatant was subjected to LC-MS/MS analysis. The MS detection was performed by using a SCIEX API 4000 QTRAP instrument. Each compound was analyzed by reverse-phase HPLC using a Kinetex 2.6 μ C18 100 Å column (3.0 mm X 30 mm, Phenomenex) with the mobile phase consisting of solvent A: water with 0.1% formic acid, solvent B: acetonitrile with 0.1% formic acid. The amount of parent compound was determined on the basis of the peak area ratio (compound area to internal standard area) for each time point. Residual enzyme activity was monitored by measuring area ratio with respect to the internal standard of the corresponding metabolite for each substrate. The IC₅₀ was fit using the GraphPad Prism software program (version 6.0) according to Equation 4:

$$\% \text{ Residual activity} = \frac{1}{1 + e^{\frac{\ln IC_{50} - \ln [I]}{P}}} \times 100 \quad (\text{Equation 4})$$

where [I] and P are inhibitor concentration and Hill slope, respectively.

Determination of Efficacy in an Intracellular Infection Model

The activity of a test compound against intracellular bacteria was determined by infecting J774.1 mouse macrophages (ATCC TIB-67) with the mc²6206 Δ leuCD Δ panCD strain of *M. tuberculosis* transformed with an mLux plasmid (kindly provided by Professor Jeffery Cox, UC Berkeley) based on published protocols (Mehta et al., 1996; Rengarajan et al., 2005). The macrophages were suspended in Dulbecco's Modified Eagle Medium (Sigma-Aldrich D6429) supplemented with 10% Fetal Bovine Serum (Sigma-Aldrich F6178) to a concentration of 2.0 x 10⁵ cells/mL. 96-well white flat-bottomed assay plates were seeded with 100 μ L of the macrophage suspension and incubated overnight to allow cells to adhere to the plate. The assay plates were then inoculated with 100 μ L of luminescent mc²6206 *M. tuberculosis* at a multiplicity of infection of 1:10. The plates were incubated for 4 h at 37°C and 5% CO₂ to allow the bacteria to infect the macrophages and then washed twice with 100 μ L of DMEM supplemented with FBS, pantothenic acid and leucine. After the second wash, 100 μ L of DMEM with gentamicin was added to each well and the plates were incubated for an additional 2 h to kill any remaining extracellular bacteria. The plates were washed twice with 100 μ L of DMEM supplemented with FBS, pantothenic acid and leucine, and then test compound was added to the plates at the desired concentrations. The plates were incubated at 37°C and 5% CO₂ for 72 h. Luminescence was measured every 24 h using the GloMax® Detection System (Promega). Each treatment was done in triplicate and the experiment was repeated twice.

100-Day Culture Methods

As seen in the Hu-Coates protocol (Hu et al., 2003), the media was obtained from Difco (Becton Dickinson Laboratories, Sparks, MD, USA) and consisted of 7H9 liquid media containing 20% Tween 80, supplemented with an albumin, dextrose, and salt (ADC) complex. Cultures of *M. tuberculosis* strain H37Rv were grown in 25 mL plastic 'Universal' Nunc™ containers with caps (Thermo Scientific, Waltham, MA, USA) incubated at 37°C placed stationary and upright in a rack for 100–115 d. After 100–115 d incubation, each tube was vortexed with sterile beads. After breaking up clumps by vortex, cultures were pooled together in single sterile flask and sonicated in a water bath (Branson Ultrasonics, CT, USA). For day 0, aliquots of pooled culture were diluted and plated on 7H11-glycerol-ADC agar plates (Becton Dickinson Laboratories, Sparks, MD, USA). In separate 'Universal' containers, drugs and DMSO (Sigma-Aldrich, St Louis, MO, USA) were prepared to final concentration of 100 μ M in triplicate. From the pooled flask, 8 mL of culture were added to new drug tubes and incubated at 37°C placed stationary and upright in a rack for 5 d. On day 5, the Nunc tubes were spun at 4000 rpm for 10 min in a Jouan CR4-12 high-speed centrifuge (Thermo Scientific, Waltham, MA, USA) and washed three times with 7H9-ADC media. After the third wash, the final pellets were resuspended with 8 mL of 7H9-ADC. CFU dilutions were prepared in 7H9-ADC media using 2 mL screw cap tubes (Fisher Scientific, Hampton, NH, USA). In between dilutions, screw-cap tubes

were vortexed and culture was pipetted vigorously to ensure recovery of cells. Dilutions were plated on 7H11-ADC agar plates and were incubated in a 37°C incubator for two - three weeks until colonies were visible. After visible growth, the colonies were counted and the CFU/mL for each test condition was determined.

Mouse Pharmacokinetics (PK) Studies

In the 5 h PK studies, two female CD-1 mice received a single dose of experimental compound administered orally at 25 mg/kg in 5% DMA/60% PEG300/35% D5W (5% dextrose in water), and blood samples were collected in K₂EDTA coated tubes pre-dose, 0.5, 1, 3 and 5 h post-dose. In iv/po PK studies, groups of three female CD-1 mice received a single dose of experimental compound administered orally at 25 mg/kg in 0.5% CMC/0.5% Tween 80 suspension, or intravenously at 5 mg/kg in 5% DMA/95% (4 % Cremophor EL). Blood samples were collected in K₂EDTA coated tubes typically 0.25, 0.5, 1, 3, 5 and 8 h post-dose in the oral arm, and typically 0.033, 0.25, 0.5, 1 and 3 h post dose in the intravenous arm. Blood was kept on ice and centrifuged to recover plasma, which was stored at -80°C until analyzed by HPLC coupled to tandem mass spectrometry (LC-MS/MS). LC/MS-MS quantitative analysis for all molecules was performed on a Sciex Applied Biosystems Qtrap 4000 triple-quadrupole mass spectrometer coupled to an Agilent 1260 HPLC system, and chromatography was performed on an Agilent Zorbax SB-C8 column (2.1x30 mm; particle size, 3.5 μm) using a reverse phase gradient elution. Milli-Q deionized water with 0.1% formic acid (A) was used for the aqueous mobile phase and 0.1% formic acid in acetonitrile (B) for the organic mobile phase. The gradient was: 5-90% B over 2 min, 1 min at 90% B, followed by an immediate drop to 5% B and 1 min at 5% B. Multiple-reaction monitoring of parent/daughter transitions in electrospray positive-ionization mode was used to quantify all molecules. Sample analysis was accepted if the concentrations of the quality control samples and standards were within 20% of the nominal concentration. Data processing was performed using Analyst software (Version 1.6.2; Applied Biosystems Sciex). Neat 1 mg/mL DMSO stocks for all compounds were first serially diluted in 50/50 acetonitrile/water and subsequently serially diluted in drug free CD-1 mouse plasma (K₂EDTA, Bioreclamation IVT, NY) to create standard curves (linear regression with 1/x² weighting) and quality control (QC) spiking solutions. 20 μL of standards, QCs, control plasma, and study samples were extracted by adding 200 μL of acetonitrile/methanol 50/50 protein precipitation solvent containing the internal standard (10 ng/mL verapamil). Extracts were vortexed for 5 min and centrifuged at 4000 rpm for 5 min. 100 μL of supernatant was transferred for HPLC-MS/MS analysis and diluted with 100 μL of Milli-Q deionized water. Mouse lungs were homogenized by adding 4 parts PBS buffer:1 part tissue and shaking the diluted samples using a SPEX Sample Prep Geno/Grinder 2010 for 5 min at 1500 rpm with steel beads. Mouse lung homogenates were processed and treated the same as plasma for compound quantification.

Mouse Acute Infection Model and Antibacterial Treatment

All mouse infection and treatment experiments were approved by the Rutgers University Institutional Animal Care and Use committee. A well-established low dose aerosol infection using a Glas-Col Inhalation Exposure System was utilized to infect inbred female Balb/C mice (19-20 g) with approximately 50-100 bacilli/mouse with *M. tuberculosis* strain H37Rv strain (Chaudhuri et al., 2018; Lan-
oix et al., 2016). At 3 h post exposure, 4 mice were humanely euthanized and lungs aseptically removed for bacterial enumeration to verify infection dose. After 14 d, 4 additional mice were humanely euthanized and lungs assessed for bacterial burdens to verify acute phase of *M. tuberculosis* infection. The remaining mice were randomized into groups consisting of 12 mice that were given single daily oral doses of vehicle (0.5% CMC/0.5% Tween-80), JSF-2513 at 200 and 60 mg/kg or INH at 25 mg/kg via oral gavage. Lungs and spleens were aseptically removed and bacterial burdens were assessed via viable counts on Middlebrook 7H11 agar supplemented with OADC on days 28 and 42 to assess treatment efficacy relative to the vehicle controls. For statistical analysis, the CFUs were converted to logarithms, and evaluated by a one-way ANOVA followed by a multiple comparison analysis of variance by Tukey and/or Dunnett's test (GraphPad Prism software program version 6.0). Differences were considered significant at the 95% level of confidence.

Determination of InhA Percent Inhibition and IC₅₀

Enzyme kinetics, following a published procedure (Sivaraman et al., 2003; Stec et al., 2014), were determined in 150 mM NaCl and PIPES buffer at pH 6.8 with a Shimadzu UV-2500 UV-visible spectrophotometer. NADH (20 μM), InhA (20 nM, expressed and purified following a literature protocol (Rawat et al., 2003)) and inhibitor (different concentrations dissolved in DMSO) were mixed and incubated for 5 min before the addition of *trans*-2-dodecenoyl-CoA (prepared from *trans*-2-dodecenoic acid, via a mixed anhydride method as described by Parikh (Parikh et al., 1999)) to initiate the reaction. Assays were followed spectrophotometrically at 25°C, tracking the consumption of NADH, to form NAD⁺. For the determination of a molecule's percent inhibition of InhA catalytic activity, the inhibitor concentration was chosen to be 50 μM. For an IC₅₀ determination, inhibitor concentrations were varied from 10 nM to 100 μM as described earlier (Freundlich et al., 2009). Equation 5 was utilized to determine the NAD⁺ production curve where N_{NAD⁺} was the NAD⁺ concentration, A₀ and A_t were the 340 nm absorbance at time t and time 0, and C_{NADH} was the initial NADH concentration.

$$N_{\text{NAD}^+} = \frac{A_0 - A_t}{A_0} \times C_{\text{NADH}} \quad (\text{Equation 5})$$

The InhA percent inhibition and/or IC₅₀ for each inhibitor were calculated with Prism GraphPad version 6.0, and reported as the mean ± standard error.

Thin-Layer Chromatography (TLC) Analysis of Fatty Acids and Mycolic Acids

Mid-log phase *M. tuberculosis* (OD₅₉₅ = 0.3) incubated at 37°C were pre-treated by compounds at different fold MIC for 8 h (5 mL culture per compound treatment) in 7H9+ADS media, and 1 μ Ci/mL of ¹⁴C-acetate (56 mCi/mmol) was added to each culture. After 16 h of ¹⁴C-acetate labeling, bacteria were harvested and washed with PBS. Bacterial lipids were hydrolyzed by incubation of the bacterial pellet with 2 mL tetra-*n*-butylammonium hydroxide (TBAH) at 100°C overnight. Fatty acids and mycolic acids were esterified by adding 4 mL CH₂Cl₂, 300 μ L CH₃I and 2 mL distilled water (ddH₂O) and mixing at rt for 1 h to generate fatty acid methyl esters (FAMES) and mycolic acid methyl esters (MAMES). After centrifugation (1500 rpm, 10 min), the upper phase was discarded, and samples were washed twice with ddH₂O. The lower phase was dried with a stream of air overnight, and FAMES/MAMES were extracted by resuspending the pellet with 3 mL diethyl ether and transferring the supernatant to new collection tubes after centrifugation (1500 rpm, 10 min). After drying the organic phase with a stream of air, the lipids were resuspended in 200 μ L CH₂Cl₂, and equal counts (50,000 cpm) were loaded on a silica gel 60 F254 thin-layer chromatography (TLC) plate and resolved using hexane/ethyl acetate (19:1, v/v, 2 runs). The FAMES and MAMES were detected by Typhoon 9400 storage phosphorimager (GE Health Sciences).

Reduction of JSF-2019 to JSF-2026

To a solution of JSF-2019 (5.0 mg, 0.012 mmol) in methanol (1.0 mL) was added sodium borohydride (4.0 mg, 0.11 mmol). The mixture was stirred at room temperature for 1 h. The reaction was monitored by LC/MS, which showed the formation of JSF-2026 by comparison with the ion extraction spectra (positive ion *m/z* 370.0) of independently synthesized JSF-2026 and via co-injection of the reaction mixture with this synthesized JSF-2026.

Synthetic Chemistry Methods

All reaction reagents were obtained from Sigma-Aldrich, Acros, Alfa Aesar, Tokyo Chemical Industry (TCI), or Fisher Scientific. The reaction solvents were purchased from either Sigma-Aldrich, Fisher Scientific, or Acros. Whenever necessary, reactions were performed under a nitrogen atmosphere and anhydrous solvents were used. Microwave reactions were performed in a CEM Discover microwave reactor. NMR spectra of the synthesized compounds were recorded on an Avance 500 MHz spectrometer from the Bruker Corporation (Billerica, MA, USA). Reverse-phase high performance liquid chromatography (HPLC) and electrospray ionization (ESI) mass spectra were obtained on an Agilent 6120 single quadrupole LC/MS system using a reverse-phase EMD Millipore Chromolith SpeedRod RP-18e column (50 \times 4.6 mm). In general, a 10 - 100% gradient of acetonitrile/water containing 0.1% formic acid was used for the analysis of the samples. All compounds were purified to \geq 95% peak area (*i.e.*, purity) via an HPLC UV trace at 220 nm or 250 nm with observation of a low-resolution MS *m/z* consistent with each compound. Purification of samples by flash chromatography was performed on a Teledyne ISCO CombiFlash Rf+ system using a Teledyne RediSep normal phase silica gel column. For TLC, aluminum plates coated by silica gel 60 with F₂₅₄ fluorescent indicator from EMD Millipore were used. Preparative reverse-phase HPLC was performed on a Varian (now Agilent) SD-1 preparative HPLC system equipped with an Agilent Pursuit (10 μ m, 250 \times 21.2 mm) C-18 column with detection UV wavelength set at 220 nm or 250 nm. A gradient of acetonitrile in water at a flow rate of 20 mL/min was used for the separation.

Synthesis of Differentially Substituted Furans JSF-2026

6-hydrazineyl-N2,N4-diphenyl-1,3,5-triazine-2,4-diamine (Ekins et al., 2013) (336 mg, 1.14 mmol) was dissolved in methanol (6.0 mL). Furfural (1.59 equiv, 1.81 mmol, 0.150 mL) was added to the reaction mixture, which was then stirred at room temperature overnight. The solvent was removed *in vacuo* and the crude material was subjected to flash column chromatography over silica gel to afford JSF-2126 as an off-white solid (169 mg, 0.456 mmol, 40.0% yield): ¹H NMR (500 MHz, d₆-DMSO) δ 10.9 (s, 1), 9.30 (br s, 1), 8.14 (s, 1), 7.81 (m, 5), 7.27 (m, 5), 6.97 (t, *J* = 10 Hz, 2), 6.76 (d, *J* = 5 Hz, 1), 6.60 (s, 1).

By a similar synthetic route the following were prepared:

JSF-2389: ¹H NMR (500 MHz, d₆-DMSO) δ 11.6 (s, 1), 9.79 (br m, 2), 8.18 (s, 1), 7.81 (s, 4), 7.34 (m, 5), 7.13 – 7.00 (m, 3). Also noted 2.00 (s), 1.93 (s), 1.24 (m), 1.19 (t), 0.96 – 0.78 (m).

JSF-2390: ¹H NMR (500 MHz, d₆-DMSO) δ 11.6 (s, 1), 9.80 (s, 2), 8.17 (s, 1), 7.78 (m, 5), 7.33 (s, 4), 7.08 (m, 3). Also noted 1.24 (s), 0.93 – 0.76 (m).

JSF-4328: ¹H NMR (500 MHz, d₆-DMSO) δ 10.9 (s, 1), 9.60 (br s, 1), 8.03 (s, 1), 7.81 (s, 1), 7.76 (br s, 2), 7.27 (t, *J* = 7.9 Hz, 2), 6.95 (t, *J* = 7.3 Hz, 1), 6.77 (d, *J* = 3.3 Hz, 1), 6.61 (dd, *J* = 3.2, 1.7 Hz, 1), 3.77 – 3.72 (m, 4), 3.68 – 3.62 (m, 4).

Syntheses of Differentially Linked Triazines JSF-2111

6-hydrazineyl-N2,N4-diphenyl-1,3,5-triazine-2,4-diamine (120 mg, 0.409 mmol) (Ekins et al., 2013) was dissolved in dichloromethane (7.0 mL). 1 N NaOH aq. (1.0 equiv, 0.410 mmol, 0.410 mL) and 5-nitrofurfuryl chloride (1.0 equiv, 0.410 mmol, 72.0 mg) were added to the reaction mixture, which was then stirred for 3 h. The resulting mixture was extracted with ethyl acetate (100 mL). The organic phase was washed with saturated aqueous brine solution (50 mL). After drying over anhydrous sodium sulfate, the organics were concentrated *in vacuo* and purified by flash column chromatography on silica gel, eluting with 0-50% ethyl acetate/hexanes, to afford JSF-2111 as a brown solid (41.0 mg, 0.0948 mmol, 23.2% yield): ¹H NMR (500 MHz, DMSO-*d*₆) δ 10.8 (s, 1), 9.44-9.18 (m, 2), 7.99-7.54 (m, 5), 7.28 (s, 2), 6.99 (t, *J*=52.1 Hz, 3), 2.88 (s, 1), 2.72 (s, 1), 1.22 (s, 1).

JSF-2113

The mixture of 5-nitrofuran-2-carbaldehyde (444 mg, 3.15 mmol) and *tert*-butyl 1-methylhydrazine-1-carboxylate (1.01 equiv, 3.18 mmol, 0.470 mL) in acetonitrile (1.0 mL) was heated at 120°C in a microwave reactor for 10 min. Then the mixture was heated at 170°C for 2 h. The resulting mixture was extracted with ethyl acetate (200 mL). The organic phase was washed with saturated aqueous brine solution (50 mL), dried over anhydrous sodium sulfate, concentrated *in vacuo*, and purified by flash column chromatography on silica gel, eluting with 0–30% ethyl acetate/dichloromethane, to afford (E)-1-methyl-2-((5-nitrofuran-2-yl)methylene)hydrazine as a red solid (300 mg, 1.77 mmol, 56.2% yield). In keeping with our standard practices, this intermediate was characterized by $\geq 95\%$ purity via HPLC and the expected parent ion via MS.

(E)-1-methyl-2-((5-nitrofuran-2-yl)methylene)hydrazine (169 mg, 1.00 mmol) was dissolved in acetonitrile (2.0 mL). Cyanuric chloride (1.0 equiv, 1.00 mmol, 185 mg) and N,N-diisopropylethylamine (2.0 equiv, 2.00 mmol, 0.348 mL) were added to the mixture at 0°C, which was then stirred at room temperature for 30 min. Aniline (2.0 equiv, 2.00 mmol, 0.182 mL) and N,N-diisopropylethylamine (2.0 equiv, 2.00 mmol, 0.348 mL) were added to the mixture, which was then heated at 120°C for 40 min. The resulting mixture was extracted with ethyl acetate (80 mL). The organic phase was washed with saturated aqueous brine solution (20 mL). After drying over anhydrous sodium sulfate, the organic solution was concentrated *in vacuo* and purified by flash column chromatography on silica gel, eluting with 0–30% ethyl acetate/dichloromethane, to afford JSF-2113 as a brown solid (128 mg, 0.298 mmol, 29.8% yield): ^1H NMR (500 MHz, CDCl_3) δ 7.72–7.59 (m, 5), 7.43 (d, J = 3.7 Hz, 1), 7.41–7.35 (m, 4), 7.13 (t, J = 7.3 Hz, 2), 7.01 (d, J = 3.2 Hz, 1), 3.68 (s, 3), 1.27 (s, 2).

JSF-2114

To a mixture of *tert*-butyl 1-methylhydrazine-1-carboxylate (0.296 mL, 2.00 mmol) in acetonitrile (10.0 mL) was added N,N-diisopropylethylamine (1.0 equiv, 2.00 mmol, 0.348 mL) and 5-nitrofurfuryl chloride (1.0 equiv, 2.00 mmol, 351 mg). The mixture was stirred at room temperature for 3 h. The resulting mixture was extracted with ethyl acetate (60 mL). The organic phase was washed with water (3 x 10 mL) and saturated aqueous brine solution (10 mL). After drying over anhydrous sodium sulfate, the solvent was removed *in vacuo* and the crude material was dissolved in dichloromethane (1 mL). Trifluoroacetic acid (1.0 mL) was added to the mixture, which was then stirred at room temperature for 1 h. The solvent was removed *in vacuo* and the crude material was subjected to flash column chromatography, eluting with 0–100% ethyl acetate/dichloromethane, over silica gel to afford N'-methyl-5-nitrofuran-2-carbohydrazide as a yellow solid (290 mg, 1.57 mmol, 78.5% yield). In keeping with our standard practices, this intermediate was characterized by $\geq 95\%$ purity via HPLC and the expected parent ion via MS.

N'-methyl-5-nitrofuran-2-carbohydrazide (50.0 mg, 0.270 mmol) was dissolved in acetonitrile (1.0 mL). Cyanuric chloride (1.0 equiv, 0.270 mmol, 49.8 mg) and N,N-diisopropylethylamine (1.0 equiv, 0.270 mmol, 0.0470 mL) were added to the mixture at 0°C, which was then stirred at room temperature for 1 h. Aniline (2.0 equiv, 0.542 mmol, 0.0490 mL) and N,N-diisopropylethylamine (2.0 equiv, 0.540 mmol, 0.0940 mL) were added to the mixture, which was then heated at 50°C for 1 h. The resulting mixture was extracted with ethyl acetate (80 mL). The organic phase was washed with saturated aqueous brine solution (20 mL). After drying over anhydrous sodium sulfate, the organic solution was concentrated *in vacuo* and purified by flash column chromatography on silica gel, eluting with 0–30% ethyl acetate/dichloromethane, to afford JSF-2114 as a brown solid (24.0 mg, 0.0538 mmol, 19.9% yield). ^1H NMR (500 MHz, CDCl_3) δ 8.76 (s, 1), 7.90–6.73 (m, 14), 3.51 (s, 3).

JSF-2116

JSF-2113 (20.0 mg, 0.0465 mmol) was dissolved in acetonitrile (1.0 mL). Sodium cyanoborohydride (3.42 equiv, 10.0 mg, 0.159 mmol) and acetic acid (0.200 mL) were added to the mixture, which was then stirred at room temperature overnight. The solvent was removed *in vacuo* and the crude material was subjected to flash column chromatography over silica gel, eluting with 0–30% ethyl acetate/dichloromethane, to afford JSF-2116 as a brown solid (4.6 mg, 0.011 mmol, 23% yield): ^1H NMR (500 MHz, CDCl_3) δ 7.56 (d, J = 7.8 Hz, 4), 7.38–7.30 (m, 5), 7.25 (d, J = 3.6 Hz, 1), 7.12 (t, J = 7.4 Hz, 2), 4.18 (s, 2), 3.32 (s, 3), 2.12 (s, 1).

JSF-2118

6-chloro-N2,N4-diphenyl-1,3,5-triazine-2,4-diamine (91.0 mg, 0.306 mmol) was dissolved in acetonitrile (1.50 mL), to which was added N,N-diisopropylethylamine (1.01 equiv, 0.310 mmol, 0.0539 mL) and *tert*-butyl 1-methylhydrazine-1-carboxylate (1.01 equiv, 0.310 mmol, 45.3 mg). The mixture was stirred at room temperature overnight. The solvent was removed *in vacuo* and the crude material was subjected to flash column chromatography over silica gel to afford *tert*-butyl 2-(4,6-bis(phenylamino)-1,3,5-triazin-2-yl)-1-methylhydrazine-1-carboxylate as a colorless liquid (112 mg, 0.275 mmol, 89.9% yield). In keeping with our standard practices, this intermediate was characterized by $\geq 95\%$ purity via HPLC and the expected parent ion via MS.

tert-butyl 2-(4,6-bis(phenylamino)-1,3,5-triazin-2-yl)-1-methylhydrazine-1-carboxylate (90.0 mg, 0.221 mmol, 1.00 equiv.) was dissolved in dichloromethane (1.00 mL), to which was added trifluoroacetic acid (0.500 mL, 6.53 mmol, 29.5 equiv). The mixture was stirred at room temperature for 1 hour. The solvent was removed *in vacuo* and the crude material was subjected to flash column chromatography over silica gel, eluting with 0–5% methanol/dichloromethane, to afford 6-(2-methylhydrazineyl)-N2,N4-diphenyl-1,3,5-triazine-2,4-diamine as a light-yellow liquid (110 mg, 0.221 mmol, >99% yield). In keeping with our standard practices, this intermediate was characterized by $\geq 95\%$ purity via HPLC and the expected parent ion via MS.

6-(2-methylhydrazineyl)-N2,N4-diphenyl-1,3,5-triazine-2,4-diamine (50.0 mg, 0.100 mmol, 1.00 equiv.) was dissolved in dichloromethane (1.00 mL), to which was added 5-nitro-2-furoic acid (35.6 mg, 0.136 mmol, 1.36 equiv), EDC (31.1 mg, 0.163 mmol, 1.63 equiv) and DMAP (20.0 mg, 0.163 mmol, 1.63 equiv). The mixture was stirred at room temperature for 1.5 hour. The resulting mixture was extracted with ethyl acetate (100 mL). The organic phase was washed with water (20.0 mL), then saturated aqueous brine solution (20.0 mL). After drying over anhydrous sodium sulfate, the organic solution was concentrated and purified by flash column

chromatography on silica gel, eluting with 0–4% methanol/ dichloromethane, to afford JSF-2118 as a brown solid (17.0 mg, 0.0381 mmol, 38% yield): ^1H NMR (500 MHz, CDCl_3) δ 7.78 – 7.00 (m, 12), 5.09 (br s, 2), 3.38 (s, 3).

Synthesis of Dialkylaminotriazines

JSF-2189

4,4'-(6-chloro-1,3,5-triazine-2,4-diyl)dimorpholine: Cyanuric chloride (900 mg, 4.88 mmol) in 25 mL dry acetonitrile under N_2 was cooled to 0°C in an ice bath. To this solution, a mixture of morpholine (932 mg, 10.7 mmol) and N,N-di-isopropylethylamine (1.70 mL, 9.76 mmol) was added dropwise over the period of 10 min. The reaction slowly increased turbidity until turning to a paste. At that time the reaction was slowly warmed to rt. The reaction was continued to stir overnight at rt and then concentrated *in vacuo* to a crude oil. The reaction mixture was purified by flash column chromatography using 0 – 50% gradient of EtOAc in hexanes to give the title compound as a white solid (1.24 g, 89.0%). In keeping with our standard practices, this intermediate was characterized by $\geq 95\%$ purity via HPLC and the expected parent ion via MS.

4,4'-(6-hydrazineyl-1,3,5-triazine-2,4-diyl)dimorpholine

To 4,4'-(6-chloro-1,3,5-triazine-2,4-diyl)dimorpholine (1.24 g, 4.34 mmol) in dry DMSO was added hydrazine monohydrate (0.842 mL, 17.4 mmol) in one portion and the reaction stirred at rt for 24 h. The reaction was slowly added to ice cold water and the crude precipitate was collected by filtration. The crude solid was washed with acetonitrile and dichloromethane to give 762 mg white solid (62.4%). In keeping with our standard practices, this intermediate was characterized by $\geq 95\%$ purity via HPLC and the expected parent ion via MS.

(E)-4,4'-(6-(2-((5-nitrofuranyl)methylene)hydrazineyl)-1,3,5-triazine-2,4-diyl)dimorpholine

To a solution of 4,4'-(6-hydrazineyl-1,3,5-triazine-2,4-diyl)dimorpholine (400 mg, 1.42 mmol) in 20 mL methanol was added 5-nitro-2-furaldehyde (210 mg, 1.49 mmol) and stirred overnight at rt. The reaction mixture was concentrated *in vacuo* and the crude product purified by flash column chromatography using a 0 – 35% gradient of acetone in dichloromethane to give the product as a crude yellow solid. A portion of the crude product (80 mg) was purified by RP-HPLC using a gradient of 30 – 75% acetonitrile in water to give 36 mg yellow solid: ^1H NMR (500 MHz, d_6 -DMSO) δ 11.3 (s, 1), 8.04 (s, 1), 7.78 (d, J = 3.9 Hz, 1), 7.11 (d, J = 3.9 Hz, 1), 3.72 (s, 8), 3.63 (d, J = 4.5 Hz, 8).

By a similar synthetic route the following were prepared:

JSF-2343: ^1H NMR (500 MHz, d_6 -DMSO) δ 11.3 (s, 1), 8.04 (s, 1), 7.78 (d, J = 3.8 Hz, 1), 7.11 (d, J = 3.6 Hz, 1), 4.03 (br s, 8), 2.62 (s, 8). Also noted 5.7 (s, DCM), 4.1 (q, EtOAc), 3.3 (s, H_2O), 2.0 (s, EtOAc), 1.1 (t, EtOAc).

JSF-2380: ^1H NMR (500 MHz, d_6 -DMSO) δ 11.1 (s, 1), 8.05 (s, 1), 7.78 (d, J = 4.0 Hz, 1), 7.14 (s, 1), 7.04 (s, 1), 6.83 (d, J = 7.6 Hz, 1), 3.79–3.64 (m, 2), 1.92–1.67 (m, 8), 1.63–1.54 (m, 2), 1.30–1.18 (m, 7), 1.15–1.06 (m, 2). One H was unaccounted for in the aliphatic region. Also noted 10.9 (br s), 4.56 (s), 3.33 (s, H_2O), 2.1 (s, acetone), 1.15 (s).

JSF-2356: ^1H NMR (500 MHz, d_6 -DMSO) δ 11.0 (d, J = 42.5 Hz, 1), 8.02 (d, J = 18.4 Hz, 1), 7.77 (d, J = 3.9 Hz, 1), 7.32 (br s, 1), 7.10 – 6.92 (comp, 2), 3.05 (t, J = 6.2 Hz, 4), 1.90 – 1.77 (m, 2), 0.86 (d, J = 6.7 Hz, 12). Also noted 3.3 (s, H_2O).

JSF-2377: ^1H NMR (500 MHz, d_6 -DMSO) δ 11.3 (s, 1), 8.08 (s, 1), 7.78 (d, J = 3.8 Hz, 1), 7.53 (s, 1), 7.29 (s, 1), 7.06 (d, J = 3.2 Hz, 1), 2.78 (m, 2), 0.68 (m, 4), 0.52 (m, 4). Also noted 5.77 (s, CH_2Cl_2), 5.03 (s), 4.03 (q, EtOAc), 3.3 (s, H_2O), 2.1 (s, acetone), 2.0 (s, EtOAc), 1.25 (s), 1.19 (t, EtOAc).

JSF-2378: ^1H NMR (500 MHz, d_6 -DMSO) δ 11.1 (s, 1), 8.04 (s, 1), 7.78 (d, J = 4.0 Hz, 1), 7.67 (s, 1), 7.32 (s, 1), 7.07 (s, 1), 4.46–4.33 (m, 2), 2.25–2.12 (m, 4), 2.04–1.91 (m, 4), 1.69–1.51 (m, 4). Also noted 11.0 (br s), 5.77 (s, DCM), 5.03 (s), 4.03 (q, EtOAc), 3.33 (s, H_2O), 2.1 (s, acetone), 1.25 (s), 1.19 (t, EtOAc), 1.15 (s).

JSF-2379: ^1H NMR (500 MHz, d_6 -DMSO) δ 11.1 (s, 1), 8.05 (s, 1), 7.78 (d, J = 3.9 Hz, 1), 7.29 (s, 1), 7.05 (d, J = 2.4 Hz, 1), 6.97 (s, 1), 4.20 (m, 2), 1.92–1.79 (br m, 4), 1.73–1.61 (br m, 4), 1.56–1.42 (br m, 8). Also noted 10.9 (s), 5.03 (s), 4.56 (s), 3.33 (s, H_2O), 2.12 (s, acetone), 1.25 (s), 1.15 (s).

JSF-2404: ^1H NMR (500 MHz, d_6 -DMSO) δ 11.1 (s, 0.7), 10.9 (s, 0.3), 8.05 (s, 1), 7.78 (d, J = 3.9 Hz, 1), 7.39–7.31 (br s, 1), 7.08–7.00 (br m, 2), 4.00–3.91 (br m, 2), 3.87 (d, J = 10.3 Hz, 4), 3.38–3.28 (br m, 4), 1.84–1.71 (m, 4), 1.56–1.46 (m, 4). Noted that the broad multiplet at 3.38–3.28 ppm overlaps with the water signal. Also noted 5.7 (s, DCM) 3.33 (s, H_2O), 1.24 (s), 0.84 (m).

JSF-2405: ^1H NMR (500 MHz, d_6 -DMSO) δ 11.2 (s, 0.7), 11.0 (s, 0.3), 8.05 (s, 1), 7.78 (d, J = 4.0 Hz, 1), 7.33–7.24 (br s, 1), 7.06 (d, J = 3.6 Hz, 1), 6.98 (d, J = 7.9 Hz, 1), 3.94–3.80 (br m, 4), 3.75 (d, J = 10.3 Hz, 2), 3.27–3.17 (br m, 2), 3.12–2.99 (br m, 2), 1.95–1.86 (br s, 2), 1.73–1.64 (m, 2), 1.58–1.47 (m, 4). Also noted 5.78 (s, DCM) 3.33 (s, H_2O), 1.24 (s), 0.84 (m).

JSF-2407: ^1H NMR (500 MHz, d_6 -DMSO) δ 11.2 (s, 1), 8.04 (s, 1), 7.77 (d, J = 3.9 Hz, 1), 7.06 (d, J = 3.9 Hz, 1), 5.00 (d, J = 60.4 Hz, 2), 2.91 (d, J = 16.1 Hz, 7), 1.12 (d, J = 6.7 Hz, 15). Integrations for methyl groups were a bit high (by 1 and 3 H). Also noted 3.3 (s, H_2O), 1.23 (s), 0.85 (s).

JSF-2511: ^1H NMR (500 MHz, d_6 -DMSO) δ 11.0 (d, J = 73.4 Hz, 1), 8.03 (d, J = 13.8 Hz, 1), 7.77 (d, J = 3.8 Hz, 1), 7.30 (br s, 1), 7.17 (s, 1), 7.04 (s, 1), 3.31 – 3.21 (m overlapped with H_2O peak, proposed 4), 2.67–2.36 (m underneath DMSO solvent peak, proposed 2), 2.06 – 1.91 (m, 4), 1.91 – 1.79 (m, 4), 1.79 – 1.58 (m, 4). Also noted 1.24 (s).

JSF-2514: ^1H NMR (500 MHz, d_6 -DMSO) δ 11.2 (d, J = 29.7 Hz, 1), 8.22 (br s, 1), 8.05 (s, 1), 7.82 (s, 1), 7.78 (d, J = 3.7 Hz, 1), 7.08 (s, 1), 5.00 – 4.92 (m, 1), 4.92 – 4.83 (m, 1), 4.73 (t, 4), 4.52 (t, J = 5.9 Hz, 4). Also noted 5.79 (s, DCM), 3.33 (s, H_2O).

JSF-2589: ^1H NMR (500 MHz, d_6 -DMSO) δ 12.2 (br s, 1), 8.14 (s, 1), 7.81 (d, J = 3.0 Hz, 1), 7.25 (s, 1), 4.15 (br s, 8), 2.32 (br s, 4).

JSF-2592: ^1H NMR (500 MHz, d_6 -DMSO) δ 11.1 (d, J = 96.6 Hz, 1), 8.05 (s, 1), 7.84 (br s, 1), 7.78 (d, J = 3.6 Hz, 1), 7.49 (s, 1), 7.07 (s, 1), 5.27 (d, J = 57.2 Hz, 2), 4.71 – 4.56 (m, 2), 2.75 – 2.25 (br m, NMR solvent + 8). Also noted 5.7 (s, DCM), 3.31 (s, H_2O), 1.24 (br s, 0.86 (m).

JSF-2594: ^1H NMR (500 MHz, DMSO) δ 11.2 (s, 1), 8.06 (s, 1), 7.77 (s, 1), 7.00 (s, 1), 5.03 – 4.61 (br s, 4), 2.85 – 2.58 (br s, 8), 2.19 – 2.01 (br s, 8), 1.92 – 1.75 (br s, 4), 1.75 – 1.57 (m, 4). Also noted 3.33 (s, H_2O).

Synthesis of mono(amine)mono(morpholine)triazines

JSF-2513

tert-butyl 2-(4,6-dichloro-1,3,5-triazin-2-yl)hydrazine-1-carboxylate. Cyanuric chloride (5.00 g, 27.1 mmol) dissolved in 100 mL dry ACN was cooled to -15°C in a salt/ice bath. To this solution, *tert*-butyl carbazate (3.77 g, 27.1 mmol) in 10 mL dry ACN was added dropwise over a period of 10 min. The reaction temperature was kept under -5°C during the addition and then slowly warmed to rt as the turbidity of the reaction increased after the addition. The reaction was continued to stir overnight at rt and then concentrated *in vacuo*. The crude product was dissolved in 150 mL EtOAc and washed with water and saturated aqueous brine solution. The organic layer was dried over anhydrous Na_2SO_4 and concentrated *in vacuo* to give 6.60 g white solid (87%). In keeping with our standard practices, this intermediate was characterized by $\geq 95\%$ purity via HPLC and the expected parent ion via MS.

tert-butyl 2-(4-chloro-6-(phenylamino)-1,3,5-triazin-2-yl)hydrazine-1-carboxylate. A suspension of *tert*-butyl 2-(4,6-dichloro-1,3,5-triazin-2-yl)hydrazine-1-carboxylate (1.00 g, 3.57 mmol) in dry THF was added N,N-diisopropylethylamine (0.746 mL, 4.28 mmol) and aniline (0.343 mL, 3.75 mmol). The reaction was stirred at rt overnight and then concentrated *in vacuo*. The reaction mixture was suspended in 100 mL EtOAc and washed with saturated aqueous NH_4Cl and saturated aqueous brine solution. The organic fraction was dried over anhydrous Na_2SO_4 and concentrated *in vacuo* to give the product as a white solid (1.19 g, 99%). In keeping with our standard practices, this intermediate was characterized by $\geq 95\%$ purity via HPLC and the expected parent ion via MS.

tert-butyl 2-(4-morpholino-6-(phenylamino)-1,3,5-triazin-2-yl)hydrazine-1-carboxylate. *Tert*-butyl 2-(4-chloro-6-(phenylamino)-1,3,5-triazin-2-yl)hydrazine-1-carboxylate (200 mg, 0.594 mmol) in 3 mL dry acetonitrile was added N,N-diisopropylethylamine (0.114 mL, 0.653 mmol), followed by morpholine (54 μL , 0.62 mmol). The reaction was stirred at rt for 24 h and concentrated *in vacuo*. The crude product was suspended in EtOAc and washed with saturated aqueous NH_4Cl and saturated aqueous brine solution. The organic layer was dried over Na_2SO_4 and purified by flash column chromatography using a gradient of 0 – 50% EtOAc in hexanes to give the title compound as a white solid (186 mg, 80.9%). In keeping with our standard practices, this intermediate was characterized by $\geq 95\%$ purity via HPLC and the expected parent ion via MS.

(*E*)-4-morpholino-6-(2-((5-nitro-2-furyl)methylene)hydrazineyl)-*N*-phenyl-1,3,5-triazin-2-amine. Acetyl chloride (92 μL , 1.3 mmol) was added dropwise to 4 mL methanol while cooling in an ice bath. The solution was warmed to rt upon addition of acetyl chloride and continued to stir for 5 min at rt. *Tert*-butyl 2-(4-morpholino-6-(phenylamino)-1,3,5-triazin-2-yl)hydrazine-1-carboxylate (100 mg, 0.268 mmol) was dissolved in this MeOH solution and stirred for 4 h at 50°C . The Boc-protected product was obtained as a white solid upon concentration *in vacuo* and was then dissolved in 5 mL methanol and 5-nitro-2-furaldehyde (51 mg, 0.29 mmol) was added. The reaction was stirred overnight at rt and concentrated *in vacuo*. The crude mixture was diluted with EtOAc and washed with saturated aqueous NaHCO_3 solution. The crude product was dried over anhydrous Na_2SO_4 and purified by flash column chromatography using a gradient of 0 – 10% methanol in dichloromethane to give the product as a dark yellow solid (93 mg, 86%): ^1H NMR (500 MHz, d_6 -DMSO) δ 11.4 (s, 1), 9.65 (s, 1), 8.09 (s, 1), 7.80 (d, J = 3.8 Hz, 3), 7.30 (t, J = 7.6 Hz, 2), 7.13 (d, J = 3.8 Hz, 1), 6.98 (t, J = 7.2 Hz, 1), 3.86 – 3.57 (m, 8).

JSF-2619

tert-butyl 2-(4-(azetidin-1-yl)-6-morpholino-1,3,5-triazin-2-yl)hydrazine-1-carboxylate. To a suspension of *tert*-butyl 2-(4-chloro-6-morpholino-1,3,5-triazin-2-yl)hydrazine-1-carboxylate (83 mg, 0.25 mmol) in 3 mL dry ACN was added DIEA (96 μL , 0.55 mmol) and azetidine HCl (26 mg, 0.28 mmol). The reaction was stirred at 50°C overnight and then concentrated *in vacuo*. The reaction mixture was suspended in 10 mL EtOAc and washed with saturated aqueous NH_4Cl and saturated aqueous brine. The organic fraction was dried over anhydrous Na_2SO_4 and concentrated *in vacuo*. The product was purified by flash column chromatography using a gradient of 0 – 70% EtOAc in hexanes to give the title compound as a white solid (49 mg, 56%). In keeping with our standard practices, this intermediate was characterized by $\geq 95\%$ purity via HPLC and the expected parent ion via MS.

(*E*)-4-(4-(azetidin-1-yl)-6-(2-((5-nitro-2-furyl)methylene)hydrazineyl)-1,3,5-triazin-2-yl)morpholine. Acetyl chloride (40 μL , 0.56 mmol) was added dropwise to 2 mL methanol with cooling in an ice bath. The solution was warmed to rt upon addition of AcCl and continued to stir for 5 min at rt. *Tert*-butyl 2-(4-(azetidin-1-yl)-6-morpholino-1,3,5-triazin-2-yl)hydrazine-1-carboxylate (49 mg, 0.14 mmol) was dissolved in this MeOH solution and stirred for 4 h at 50°C . The Boc-protected product was obtained as a white solid upon concentration *in vacuo*. Without further purification, the crude product was dissolved in 2 mL methanol and 5-nitro-2-furaldehyde (23 mg, 0.16 mmol) was added. The reaction was stirred overnight at rt and concentrated *in vacuo*. The crude mixture was dissolved in EtOAc and washed with saturated aqueous NaHCO_3 solution. The crude product was dried over anhydrous Na_2SO_4 and purified by flash column chromatography using a gradient of 0 – 5% methanol in dichloromethane to give the product as a yellow solid (34 mg, 62%): ^1H NMR (500 MHz, d_6 -DMSO) δ 11.3 (s, 1), 8.03 (s, 1), 7.77 (d, J = 3.9 Hz, 1), 7.09 (d, J = 4.0 Hz, 1), 4.02 (t, J = 6.8 Hz, 4), 3.78 – 3.66 (m, 4), 3.66 – 3.53 (m, 4), 2.32 – 2.21 (m, 2).

JSF-2625

4-hydrazineyl-*N*-(1-methylcyclopropyl)-6-morpholino-1,3,5-triazin-2-amine. To a solution of 4-(4,6-dichloro-1,3,5-triazin-2-yl)morpholine (150 mg, 0.638 mmol) in dry acetonitrile at 0°C were added N,N-diisopropylethylamine (122 μL , 0.702 mmol) and

1-methyl-cyclopropanamine HCl (69 mg, 0.638 mmol). The reaction was allowed to warm to rt and stirred overnight. The reaction mixture was concentrated *in vacuo* and the residue was taken up in 25 mL EtOAc. The organic layer was washed with saturated aqueous NH₄Cl and saturated aqueous brine solution. The organic layer was dried over anhydrous Na₂SO₄ and concentrated *in vacuo*. The intermediate was obtained as crude white solid with >95% purity by LC/MS analysis. The crude solid was dissolved in 4 mL methanol and hydrazine hydrate (123 μ L, 2.55 mmol) was added in one portion. The reaction was stirred at rt for overnight and then concentrated *in vacuo*. A white solid was obtained in quantitative yield (336 mg). In keeping with our standard practices, this intermediate was characterized by \geq 95% purity via HPLC and the expected parent ion via MS.

(*E*)-*N*-(1-methylcyclopropyl)-4-morpholino-6-(2-((5-nitrofuran-2-yl)methylene)hydrazineyl)-1,3,5-triazin-2-amine. To a solution of 4-hydrazineyl-*N*-(1-methylcyclopropyl)-6-morpholino-1,3,5-triazin-2-amine (336 mg, 1.26 mmol) in 5 mL methanol was added 5-nitro-2-furaldehyde (197 mg, 1.39 mmol). The reaction was stirred overnight at rt and concentrated *in vacuo*. The crude product was suspended in 25 mL EtOAc and washed with saturated aqueous NH₄Cl and saturated aqueous NaHCO₃ solutions. The crude product was dried over anhydrous Na₂SO₄ and purified by flash column chromatography using a gradient of 0 – 5% methanol in dichloromethane to give the product as a yellow solid (189 mg, 76% over 3 steps): ¹H NMR (500 MHz, d₆-DMSO) δ 11.22 (s, 0.25), 11.16 (s, 0.68), 8.22 (s, 0.28), 8.02 (s, 0.82), 7.77 (d, *J* = 3.0 Hz, 1), 7.72 (s, 1), 7.32 (s, 0.22), 7.07 (s, 0.91), 3.75 (s, 4), 3.65 (s, 4), 1.37 (s, 3), 0.70 (s, 2), 0.56 (s, 2).

QUANTIFICATION AND STATISTICAL ANALYSIS

Data were presented as means \pm standard error determined from biological triplicates. Statistical analysis was performed with GraphPad Prism (version 6.0). Results in Figures 2B, 2C, 3B, and 3C were analyzed by paired Student's t-test. Results in Figures 2D, 2E, 2F, 3D, and 3E were analyzed by paired multiple t-tests corrected for multiple comparison using the Holm-Sidak method. Results in Figure S3E were analyzed with the unpaired Student's t-test. BRAID analysis regarding drug-drug interactions (Figure S2) was performed via R package 'braidr', and interactions were categorized as antagonism ($\kappa < 0$), no interaction (neither synergy nor antagonism) ($\kappa = 0$) or synergy ($\kappa > 0$). The heatmaps (Figures 2G, 2H, and 4A) were generated and analyzed via R package 'pheatmap' by hierarchical clustering with Euclidean distance. The grey scale quantification (Figures 3H, 3I, and 4D) was performed with ImageJ.

DATA AND CODE AVAILABILITY

Whole-genome sequencing data for the *M. tuberculosis* mutants in this paper have been deposited in the NCBI Sequence Read Archive (SRA) with access code PRJNA521574. RNAseq data for *M. tuberculosis* strains in this paper have been deposited to NCBI Gene Expression Omnibus (GEO) with access code GSE126718.